Thesis for the Degree of Doctor of Philosophy
In
Thermo and Fluid Dynamics

Analytical and Numerical Studies of Internal Swirling Flows

Walter Gyllenram

Division of Fluid Dynamics

Department of Applied Mechanics

Chalmers University of Technology

Göteborg, Sweden, 2008

Analytical and Numerical Studies of Internal Swirling Flows
WALTER GYLLENRAM
ISBN 978-91-7385-104-6

Doktorsavhandling vid Chalmers tekniska högskola
Ny serie nr 2785
ISSN 0346-718X

Division of Fluid Dynamics
Department of Applied Mechanics
Chalmers Tekniska Högskola
SE-412 96 Göteborg
Sweden
Phone +46-(0)31-7721400
Fax: +46-(0)31-180976

Cover: Iso-surfaces of the second invariant of the velocity gradient tensor in a swirling flow through a sudden expansion. The colours represent the level of static pressure, where blue corresponds to the lowest level.

This document was typeset using LaTeX

Printed at Chalmers Reproservice, Göteborg, Sweden 2008

Analytical and Numerical Studies of Internal Swirling Flows

WALTER GYLLENRAM

Division of Fluid Dynamics
Department of Applied Mechanics
Chalmers University of Technology

Abstract

Swirling flows are common in technical applications, e.g. turbines, pumps, fans, compressors and combustors. The objectives of the present work are to acquire an understanding of the physics of swirling flow in general and unsteady swirling flow in draft tubes of hydro turbines in particular, and to find a simulation method suitable for industrial purposes.

An analysis was made of the quasi-cylindrical approximation of the Navier-Stokes equations. The analysis shows that there are no quasi-cylindrical solutions at certain critical levels of swirl. Furthermore, it is shown that this property of the equations is connected to the vortex breakdown phenomenon, i.e. the sudden change of flow structure often observed in swirling flow. In draft tubes in hydraulic power plants, a vortex breakdown gives rise to a precessing vortex core that induces a temporally periodic load on the machine, which in turn causes bearing wear and increases the risk of fatigue failure.

An industrially applicable hybrid LES/RANS method was generalized and employed. The hybrid method is based on a dynamic filtering procedure of the turbulent length and time scales obtained from an eddy-viscosity RANS turbulence model. The method has been used for detailed investigations of the dynamic behaviour of swirling flows through a sudden expansion and a hydro turbine draft tube. It is shown that the filtering procedure yields solutions that contain accurate unsteady information. In addition, the time-averaged results obtained using the filtered model are significantly better than those obtained using other hybrid methods and unsteady RANS simulations.

Keywords: Swirling flow, vortex, draft tube, hydro turbine, LES, RANS, filter, turbulence.

List of Publications

This thesis is based on the work contained in the following papers:

Paper I W. Gyllenram, H. Nilsson and L. Davidson
"On the failure of the quasi-cylindrical approximation and the connection to vortex breakdown in turbulent swirling flow"
Physics of Fluids, 19:4, 2007.

Paper II W. Gyllenram and H. Nilsson
"Design and validation of a scale-adaptive filtering technique for LRN turbulence modeling of unsteady flow"
Accepted for publication in Journal of Fluids Engineering, 2008

Paper III W. Gyllenram and H. Nilsson
"The influence of boundary layers on the critical swirl level and stability of viscous swirling flow"
Submitted to scientific journal, 2008.

Paper IV W. Gyllenram, P. Stein and H. Nilsson
"Assessment of a hybrid LES/RANS turbulence model in unsteady swirling and recirculating flow"
Submitted to scientific journal, 2008.

Division of work between authors and contributors

The respondent is the first author of all papers on which this thesis is based. The respondent produced all the results, including the theoretical parts, with the exceptions explicitly mentioned in this section. The objectives of the research presented, and the contents of each paper,

have been discussed in detail with the corresponding co-author(s), who provided valuable comments.

In the work described in Paper I, the results ascribed to Rusak et al. were digitally extracted from a scan of a figure in the paper by Rusak et al. referred to in Paper I.

The numerical simulations described in Paper II were carried out using an in-house code, written and developed by Prof. Lars Davidson and Dr. Håkan Nilsson, Chalmers University of Technology. The experimental data used for validation of the numerical results were produced by Dr. Paul A. Dellenback, University of Wyoming, USA. The same data were used in Paper IV.

The results of the simulation using the Reynolds stress model shown in Paper IV were produced by Dr. Peter Stein, VA Tech Hydro, Switzerland. Dr. Stein also provided the block structure of the draft tube grid, which was used as a basis for the new grid that was developed in Paper IV. The experimental data used for validation of the draft tube test case were provided by VA Tech Hydro, Switzerland.

The commercial software used by the respondent during the work of this thesis include CEI Ensight, Fluent, Gambit, ICEM CFD, and MATLAB.

Other relevant publications

W. Gyllenram and H. Nilsson, "Very large eddy simulation of draft tube flow", *Proc. 23rd IAHR Symposium*, Yokohama, Japan, Oktober 2006.

W. Gyllenram, H. Nilsson and L. Davidson, "Large eddy simulation of turbulent swirling flow through a sudden expansion", *Proc. 23rd IAHR Symposium*, Yokohama, Japan, Oktober 2006.

W. Gyllenram, *Analytical and numerical investigations of steady and unsteady turbulent swirling flow in diffusers*, Thesis for the Degree of Lic. Eng., Chalmers University of Technology, Göteborg, Sweden, April 2006.

Acknowledgements

This work was conducted at the Division of Fluid Dynamics, Department of Applied Mechanics, Chalmers University of Technology.

The research presented in this thesis was carried out as a part of the Swedish hydropower centre (SVC). SVC was established by the Swedish Energy Agency, Elforsk and Svenska Kraftnät together with Luleå University of Technology, the Royal Institute of Technology, Chalmers University of Technology and Uppsala University. Participating companies are Alstom, CarlBro, E.ON Vattenkraft Sverige, Fortum Generation, GE Energy (Sweden) AB, Grontmij, Jämtkraft, Jönköping Energi, Mälarenergi, Skellefteå Kraft, Sollefteåforsens, Statoil Lubricants, Sweco VBB, Sweco Energuide, SweMin, Tekniska Verken i Linköping, Vattenfall Research and Development and Vattenfall Vattenkraft, Waplans, VG Power and Öresundskraft. The financial support of SVC is gratefully acknowledged.

I would like to acknowledge the Swedish National Infrastructure for Computing (SNIC) and Chalmers Center for Computational Science and Engineering (C^3SE) for providing computational resources, and Fluent Sweden AB for providing software licenses.

I would like to thank my supervisors, Dr. Håkan Nilsson and Prof. Lars Davidson, for their support and guidance during this work.

Finally, I would especially like to acknowledge my colleagues and all other employees at the Division of Fluid Dynamics for creating a stimulating working atmosphere.

Nomenclature

All symbols whose identity is not obvious are identified the first time they appear in the text, and at all subsequent times when confusion might otherwise arise. The following nomenclature should merely be regarded as a complement. The appended papers may have a slightly different notation.

Roman

A	Area
$\mathbf{a}$	Acceleration vector
c_{w1}, c_{w2}	Model constants
D	Diameter
e	Energy
$\mathbf{F}$	Force vector
g	Gravitational acceleration
H, h	Head
k	Turbulent kinetic energy
L	Length scale
M	Angular momentum or Mach number
m	Mass
n_i	Normal vector
P, p	Pressure
Q	Volume flow rate
R	Radius
Re	Reynolds number
r	Radial coordinate
S	Swirl
S_{ij}	Strain rate tensor
T_t	Turbulent time scale
U, V, W	Characteristic velocity (U) or velocity components
$\mathbf{u}$, u_i	Velocity vector
V_r, V_θ, V_z	Velocity components in cylindrical coordinates
z	Axial coordinate in cylindrical coordinates

Super- and Subscripts

abs	Absolute
atm	Atmospheric
cl	Centerline
$crit$	Critical
i, j, k	Principal directions or tensor indices
$loss$	Loss
opt	Optimal
p	Pressure
θ	Tangential direction
r	Radial direction
sgs	Subgrid scale
t	Turbulent
x, y, z	Spatial directions or derivatives

Greek

α	Swirl correction factor
β	Model constant
γ	Half opening angle,
Δ	Grid scale
δ	Boundary layer thickness
δ_{ij}	Kroneckers delta tensor
δt	Time step
δV	Grid cell volume
ε	Dissipation of turbulent kinetic energy
η	Efficiency
θ	Tangential direction
κ	von Karman's constant
$\Lambda,\ \lambda$	Characteristic length scales
μ	Dynamic molecular viscosity
μ_t	Dynamic eddy-viscosity (turbulent viscosity)
ν	Kinematic molecular viscosity
ν_t	Kinematic eddy-viscosity (turbulent viscosity)
ρ	Density
$\sigma_k,\ \sigma_w$	Model constants
τ_{ij}	Shear stress tensor
Ω	Angular velocity
ω	Specific dissipation
Ψ, ψ	Stream function

Abbreviations

S-A	Spalart-Allmaras
CFD	Computational Fluid Dynamics
DES	Detached Eddy Simulation
DNS	Direct Numerical Simulation
LES	Large Eddy Simulation
LRN	Low Reynolds Number
RANS	Reynolds Averaged Navier-Stokes
RSM	Reynolds Stress Model
SST	Shear Stress Transport
TWL	Tail Water Level

Mathematical operators and symbols

∇	Gradient operator
D_0	Total (material) derivative; $\partial_0(\cdot) + u_j \partial_j(\cdot)$
d_0	Time derivative
∂_0	Partial time derivative
d_i, d_j	Spatial derivatives in principal directions
∂_i, ∂_j	Partial spatial derivatives in principal directions
∂_z	Partial spatial derivative in the axial direction
$(\cdot)$	Arbitrary quantity
$\widehat{(\cdot)}$	Integrand variable or filtered quantity
$\overline{(\cdot)}$	Averaged quantity

Contents

Chapter 1

Background

The electrical power produced by a hydraulic power plant originates from the sun. The sun's heat on the earth's surface and atmosphere drives ocean currents, winds and the vaporization of water. Atmospheric water is transported to inland areas and mountains by wind, where it condenses and accumulates in lakes and rivers.

In the shadow of the climate change and other disadvantages related to the use of fossil energy, hydropower appears to be one of the most appealing alternatives for energy production. It is a 100% renewable energy source. In addition, hydro turbines in operation create almost no pollution and leave behind no waste. The main drawback is the environmental impact of the dam and the reservoir. Apart from limiting the mobility of wild life and physically changing riverbanks, the dam will affect the environment and the ecosystem in many other respects. In filling up the reservoir, land-based plant material is sometimes covered by water. When this biomass breaks down it produces greenhouse gases, see e.g. Fearnside [1]. The reservoir created by the dam sometimes also has a social impact. From an energy production point of view, however, the reservoir is one of the chief advantages of a hydropower plant because of its unique ability to store energy and to handle seasonal and daily peak loads. The reservoir accumulates water during periods of low energy consumption, which can later be used to provide power at periods of high energy consumption.

Hydropower is presently the second largest source of renewable energy on earth. It supplies approximately 16% of the world's electricity [2], and generates approximately 40% of the electrical power in Sweden [3]. An overview of a hydraulic power plant is shown in Fig. 1.1. The potential energy of the dammed water is proportional to the static head, and is converted to kinetic energy by the work of gravity. The kinetic energy of the running water is in turn converted to mechanical energy of the runner. The runner is mounted to the rotor axis

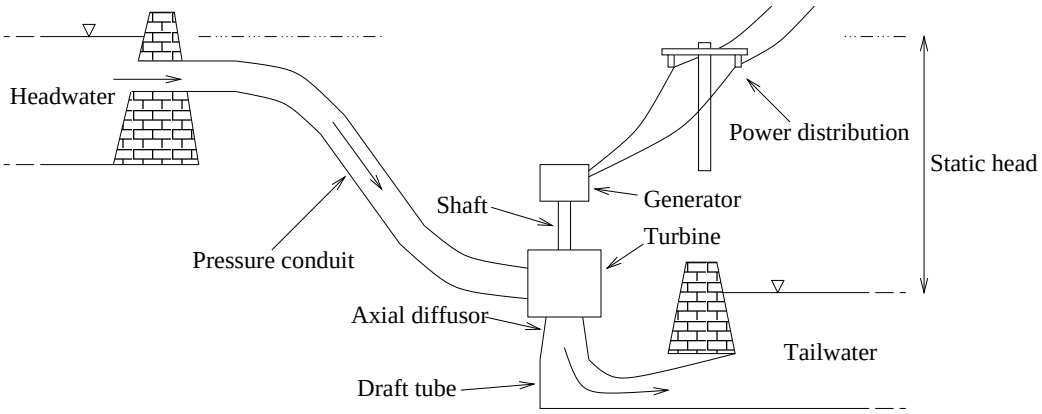

FIGURE 1.1: An overview of a hydraulic power plant.

of a generator, which finally converts the energy to electricity. There are various types of hydro turbines. The most common types are the Kaplan, Francis and Pelton turbines, each of which is named after its inventor.[1] Figure 1.2 (to the left) shows a Kaplan turbine. The adjustable blades of the Kaplan runner give the turbine a relatively wide operational range. It is the most efficient turbine at low and varying head, and is also the most common type of turbine in Sweden. A Francis turbine usually operates at higher head, in a range of ten meters to several hundred meters. Contrary to the Kaplan turbine, the flow enters the Francis runner radially instead of axially. At very high head, the Pelton turbine is the most efficient type. The Pelton turbine resembles a paddle wheel but is characterized by an advanced hydrodynamic design, just like the other types.

Downstream of the runner in hydraulic power plants of the Francis or Kaplan type, the flow exits the turbine through a draft tube. The draft tube acts as a diffuser. Its purpose is to reduce the exit velocity with a minimum loss of energy. The decelerating flow will induce a low static pressure in the region just downstream of the runner (see Chapter 2). The low pressure increases the flow rate and, consequently, the output power of the turbine. The efficiency of the draft tube is very important for a hydro turbine working at low head and it is determined by how well the flow responds to the geometry. The design of many draft tubes in use today is far from optimal. There is thus a high demand for hydrodynamical competence in this area.

Swedish hydro turbines sometimes operate at part load conditions, for which they are not designed. The main reason for this is the deregulation of the Swedish energy market, i.e. that the operational flexibil-

[1]Viktor Kaplan (1876-1934), James Francis (1815-1892), and Lester Pelton (1829-1908).

ity of hydro turbines must be utilized to compensate for varying loads on the transmission grid. For reasons explained in the following section, the flow at part load condition sometimes creates hydrodynamical problems. It is necessary to be able to find the operational limits of a turbine, and the range for which the turbine operates safely and efficiently. This calls for accurate simulation methods.

1.1 Swirling flow in hydro turbines

A swirling flow is created in the spiral casing and wicket gate, just upstream of the runner, see Fig. 1.2 (to the left). The runner rotates in the same direction as the flow. Because of the angle of the runner blades, in combination with the rotational speed of the runner, the swirl will be more or less completely neutralized when the turbine operates at full load, i.e. at its design point. However, at part load operation, a strongly swirling flow exits the runner in the form of a large vortex. The vortex often forms a helicoidal flow field that rotates around the geometrical axis of the draft tube cone, see Fig 1.2 (to the right). The precessing helicoidal vortex induces a periodic pressure load, which causes, e.g., bearing wear and increases the risk of fatigue failure. In order to improve the hydrodynamical design of the turbine it is necessary to acquire an understanding of the vortex dynamics and to be able to accurately simulate the dynamics of the unsteady swirling flow.

1.2 Objectives and delimitations

The objectives of the present work are to acquire an understanding of the physics of swirling flow in general and unsteady swirling flow in draft tubes of hydro turbines in particular, and to find a simulation method that is applicable for industrial purposes.

Despite the simple geometry of a hydro turbine draft tube, the flow shows a high degree of complexity at off-design conditions. It is a swirling, unsteady, partly separated and recirculating flow that enters the draft tube through a rotating runner. In addition, the flow moves against an opposing pressure gradient and through a sharp bend. The work in this thesis deals to a large extent with swirling flows in slightly simplified geometries, i.e. geometries containing neither the runner nor the sharp bend, in order to isolate and study the most important physical aspects of the swirling flow itself. The flow through the runner or upstream thereof has not been studied.

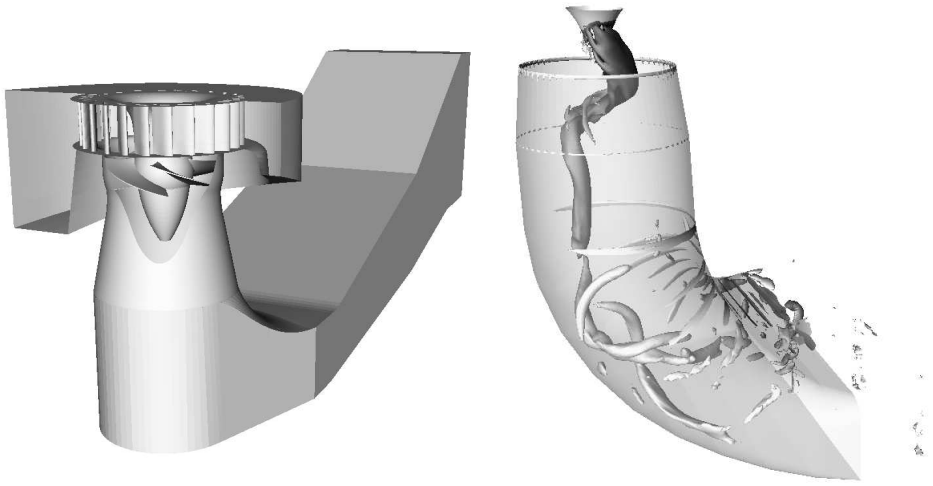

FIGURE 1.2: Left: The geometry of the Kaplan turbine at Hölleforsen including the spiral casing, the wicket gate (guide vanes), the runner and the draft tube. Right: A rotating vortex core in a draft tube, visualized by an isosurface of the second invariant of the velocity gradient tensor. The results are obtained at part load conditions, $Q/Q_{opt} = 0.71$, where Q_opt is the discharge at the optimal operating point. It rotates around the geometrical symmetry axis with a well-defined frequency. A structure resembling a double helix is formed in the bend.

1.3 Outline of the thesis

This thesis is based on four appended papers, of which two have been published or accepted for publication in well known scientific journals. The two most recently written papers have yet only been submitted to scientific journals. All research results are included in the papers, which are briefly summarized in Chapter 4. In order to make the scope of the thesis comprehensible for a wider audience, the following two chapters are dedicated to non-experts of fluid dynamics.

Chapter 2

The Flow in a Draft Tube

The purpose of the draft tube is to improve the efficiency of the hydro turbine. By converting as much as possible of the kinetic energy of the water coming into the draft tube to static pressure, the draft tube can make use of a large part of the energy that exits the runner. Practically, the conversion is done by the streamwise increase in the cross-sectional area of the draft tube. The flow decelerates quadratically with an increase in cross-sectional area because of conservation of mass, and the pressure must thereby increase until it reaches the pressure level of the tail water. A highly simplified mathematical explanation of how the energy is recovered follows in Section 2.1. The simplified analysis implicitly assumes near-optimal flow conditions, i.e. where most of the swirl has been removed by the runner (see Section 1.1). At part load operation, however, the complexity of the flow drastically increases because of the swirl. The origins of the complex dynamics of the swirling flow can — at least partly — be understood by the physical reasoning and the analytical tools presented in Section2.2. The higher complexity of the swirling flow calls for much more advanced (numerical) methods in order to get a fair approximation of, for instance, the energy recovery. These methods will be discussed in Chapter 3.

2.1 The flow at near-optimal conditons

The analysis in this section is based on the Bernoulli[1] equation, which can be interpreted as the energy equation along a streamline for an incompressible flow. With few exceptions, the analysis follows the outline of Krivchenko [4].

A sketch of a simplified draft tube is shown in Fig. 2.1. The flow enters the draft tube with velocity V_0 at depth z_0 below the tail water

[1]Daniel Bernoulli, 1700-1782

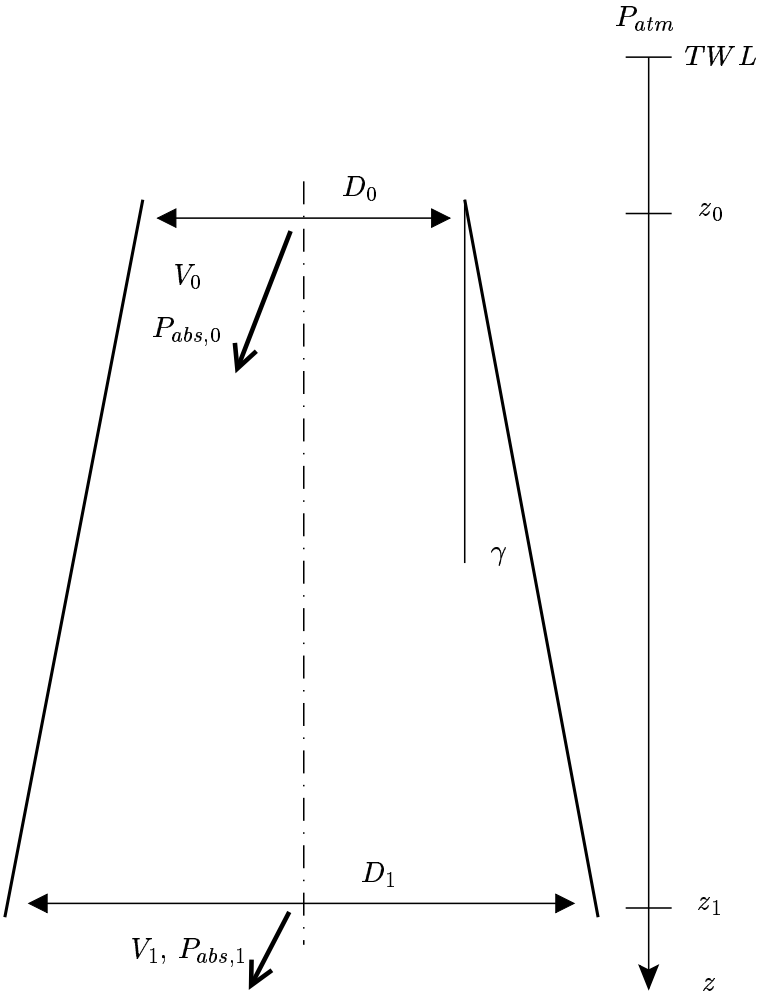

FIGURE 2.1: A sketch of a simplified hydro turbine draft tube; a vertical diffuser. The flow enters the draft tube at the top, at velocity V_0. The inlet of the draft tube is usually below the tail water level. At the outlet of the draft tube, at depth z_1, the velocity has decreased to V_1 because of the increasing cross-sectional area of the draft tube. D_0 and D_1 are the inlet and the outlet diameters of the draft tube, respectively, and γ is the half opening angle.

level[2]. The flow decelerates as it moves through the draft tube and exits with velocity V_1, at depth z_1 below the tail water level. The Bernoulli equation between the inlet and the outlet of the draft tube reads

$$P_{abs,0} - \rho g z_0 + \rho V_0^2/2 = P_{abs,1} - \rho g z_1 + \rho V_1^2/2 + \rho g h_{loss}, \qquad (2.1)$$

where $P_{abs,0}$ and $P_{abs,1}$ denote the absolute pressures at the inlet and

[2]The risk of cavitation problems in the draft tube is smaller the deeper it is located, because of the higher pressure level.

outlet of the draft tube, respectively, and g is the gravitational acceleration. The head loss in the draft tube is denoted by h_{loss}. The Bernoulli equation can also be applied between a point outside the draft tube, at the same depth as the outlet, and an arbitrary point at the tail water surface,

$$P_{abs,1} = P_{atm} + \rho g z_1. \tag{2.2}$$

Naturally, the absolute pressure at the tail water surface equals the atmospheric pressure, and the absolute pressure at any point located at the same depth as the outlet of the draft tube equals $P_{abs,1}$. The velocities can be considered negligible at any point outside the draft tube because of the large surface area. By substituting the term $P_{abs,1}$ in Eq. (2.1) for the right hand side of Eq. (2.2), we get

$$P_{abs,0} = P_{atm} - \rho \left(V_0^2 - V_1^2\right)/2 + \rho g(z_0 + h_{loss}). \tag{2.3}$$

The larger the area ratio, $A_1/A_0 = D_1^2/D_0^2$, between the outlet and inlet cross-sections of the draft tube, the larger the difference between inlet and outlet velocities and the lower the absolute pressure, $P_{abs,0}$, induced just downstream of the runner. A lower pressure induced at the inlet of the draft tube will create a higher flow rate, Q. Because the available power is proportional to the flow rate, the draft tube will significantly increase the output power of the turbine.

For a fixed draft tube length, the area ratio, A_1/A_0, is determined by the (half) opening angle, γ, see Fig. 2.1. However, the half opening angle can usually not be much larger than $10°$ because of the risk of flow separation at the draft tube walls, which would dramatically decrease the efficiency.

2.1.1 The draft tube efficiency

The energy loss (per unit volume) out from the draft tube is

$$e_0 = \rho V_1^2/2 + \rho g h_{loss}. \tag{2.4}$$

The energy loss without the draft tube is

$$e_0' = \rho V_0^2/2 + \rho g z_0. \tag{2.5}$$

The energy saved is thus

$$e_0' - e_0 = \rho \left(V_0^2 - V_1^2\right)/2 + \rho g(z_0 - h_{loss}). \tag{2.6}$$

In other words, the energy savings are proportional to the difference between the inlet and outlet kinetic energy of the flow. The ratio of the

energy savings to the kinetic energy that enters the draft tube is the energy recovery, or efficiency of the draft tube, η. It reads

$$\begin{aligned} \eta &= \frac{e_0' - e_0 - \rho g z_0}{\rho V_0^2/2} \\ &= \frac{V_0^2 - V_1^2 - 2gh_{loss}}{V_0^2}. \end{aligned} \tag{2.7}$$

A typical efficiency of a draft tube is $\eta \sim 80\%$. However, the efficiency is very sensitive to the flow rate and swirl level. If the hydro turbine operates at part load, say $Q/Q_{opt} = 90\%$, the draft tube efficiency may drop below 45% [5]. Furthermore, the relative importance of the draft tube for the overall machine efficiency increases the lower the total head. The hydrodynamical design of the draft tube is thus essential for many Swedish hydropower plants.

The next section will discuss the hydrodynamical phenomena that occur in the draft tube at part load conditions. Hopefully it will also shed some light on why the draft tube efficiency is so sensitive to the flow rate.

2.2 The flow at part load operating conditions

As mentioned in Section 1.1, a swirling flow is created in the spiral casing and wicket gate, just upstream of the runner. The runner blades will more or less neutralize the swirling part of the flow if the turbine is operating at its design point. A weak swirl is sometimes allowed to enter the draft tube in order to stabilize the flow and to prevent flow separation at the draft tube walls, but any swirl downstream of the runner is generally considered an energy loss. At part load conditions, the guide vanes are turned to decrease the flow rate, and thus a higher level of swirl is created upstream of the runner. Because the runner blades are not designed for this swirl level, the flow will exit the runner in the form of a large vortex. This chapter briefly discusses how the geometry of the draft tube influences the evolution of the part load vortex.

2.2.1 Vortex breakdown in a draft tube

The relative swirl level of a vortex increases at it moves through the draft tube. At high enough a swirl level, a vortex will break down. A vortex breakdown can be defined as a sudden change of flow structure.

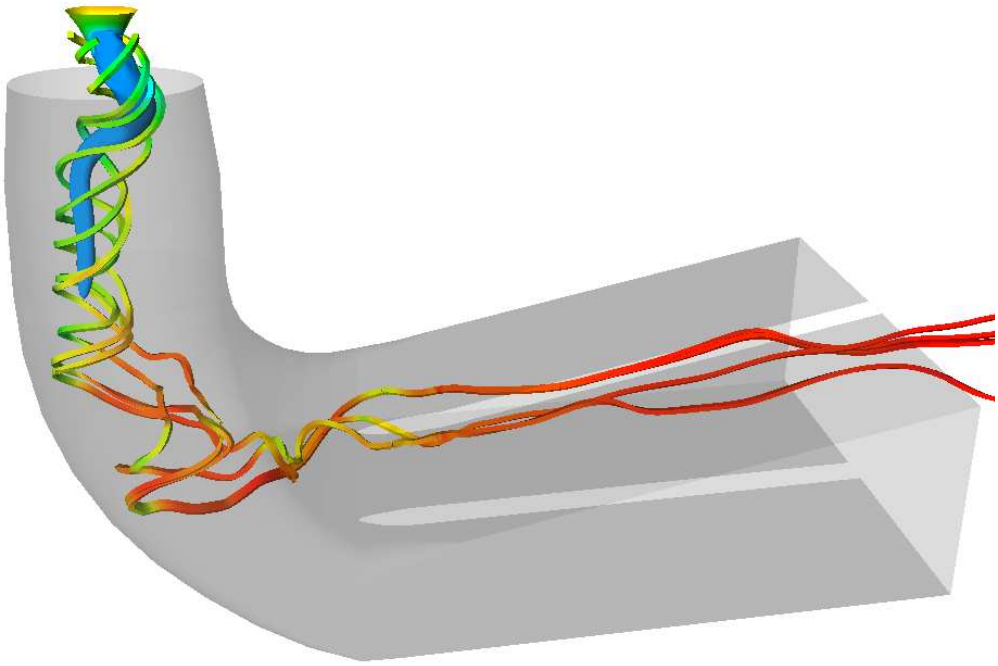

FIGURE 2.2: Snapshot of a precessing vortex core in a draft tube, visualized by an iso-surface of static pressure. The flow enters the draft tube at the top, with a clockwise swirl. Four streamlines are shown, which describe the particle paths around the vortex core if the flow was frozen at this instant. The runner hub, the iso-surface, and the streamlines are coloured by the static pressure. Blue colour denotes the lowest pressure. The simulation was made at part load conditions, $Q/Q_{opt} = 0.71$, where Q_{opt} is the discharge at the optimal operating point.

At a critical swirl level, a steady quasi-cylindrical flow can almost instantly transform into a highly unsteady, asymmetric and recirculating flow. There is no universal value for the critical swirl level, as there is no single parameter that fully defines an arbitrary swirling flow. Experimental visualizations of vortex breakdown in pipes at low Reynolds numbers, e.g. the work of Sarpkaya [6] and Mattner et al. [7], show that the initial flow structure of a vortex breakdown often resembles a bubble. The vortex breakdown bubble is formed when a quasi-cylindrical flow suddenly develops large positive radial velocities near the symmetry axis. If the radial velocities are large enough, a free stagnaton point may form. The outer part of the flow is accelerated because of conservation of mass, while the inner part of the flow starts to recirculate in the region just downstream of the stagnation point. Because the vortex breakdown bubble is very unstable, its life span is usually very short. The bubble structure will eventually transform into a highly un-

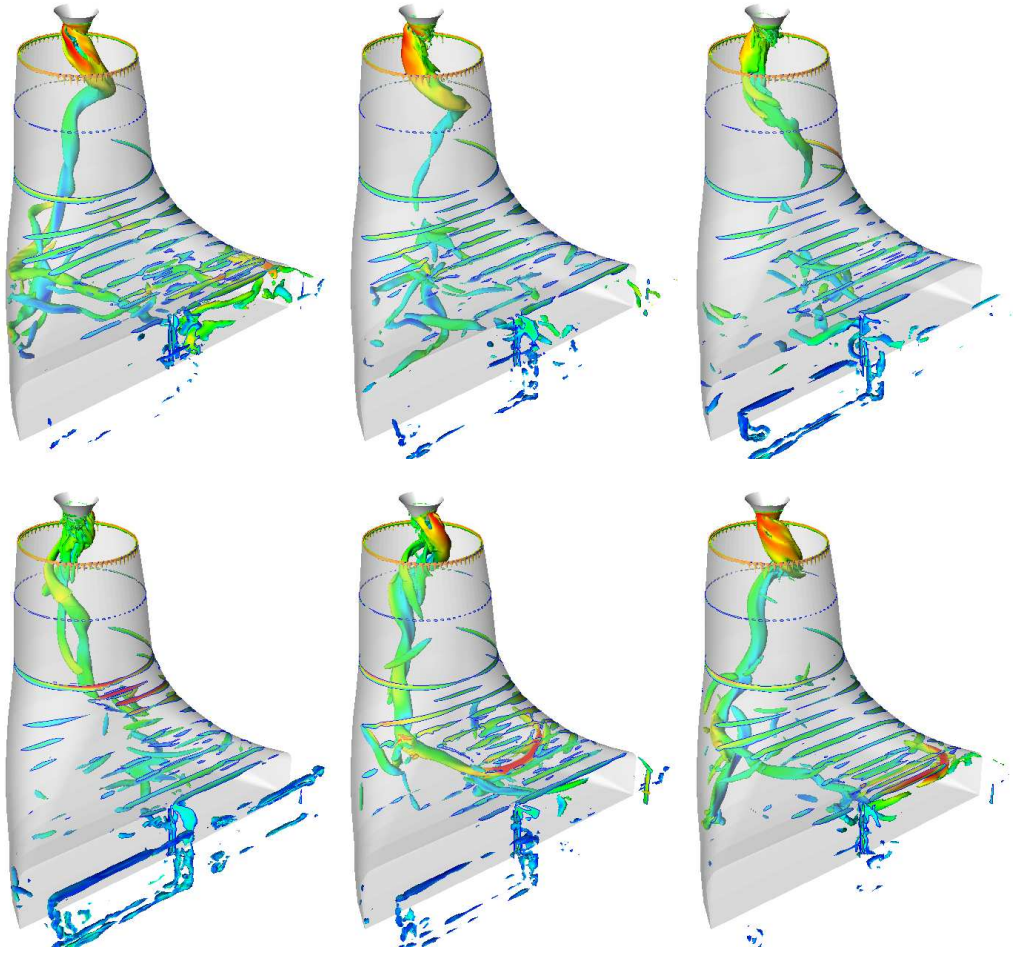

FIGURE 2.3: Row-wise from top: Six snapshots of a precessing vortex core in a draft tube operating at part load, visualized by positive iso-surfaces of the second invariant of the velocity gradient tensor. The inlet swirl is clockwise if viewed from above, and the time lag between each snapshot corresponds to one full runner rotation. In this particular case $f_v/f_n \approx 0.2$, where f_v and f_n are the rotational frequency of the vortex core and the runner, respectively. The colours represent the magnitude of the velocity vector, where red corresponds to the highest velocity.

steady flow. Many times, as is the case in draft tube flow, the vortex breakdown results in a helicoidal vortex structure that rotates around the symmetry axis of the draft tube cone, as well as around its own axis, see Figs. 2.2 - 2.5. The six snaphots in Fig. 2.3 show that the rotational frequency of the vortex rope, f_v, is much lower than the rotational frequency of the runner, f_n. In this particular case $f_v/f_n \approx 0.2$. The rotating structure will induce vibrations and unsteady loads on the runner hub and draft tube walls because of the low pressure region

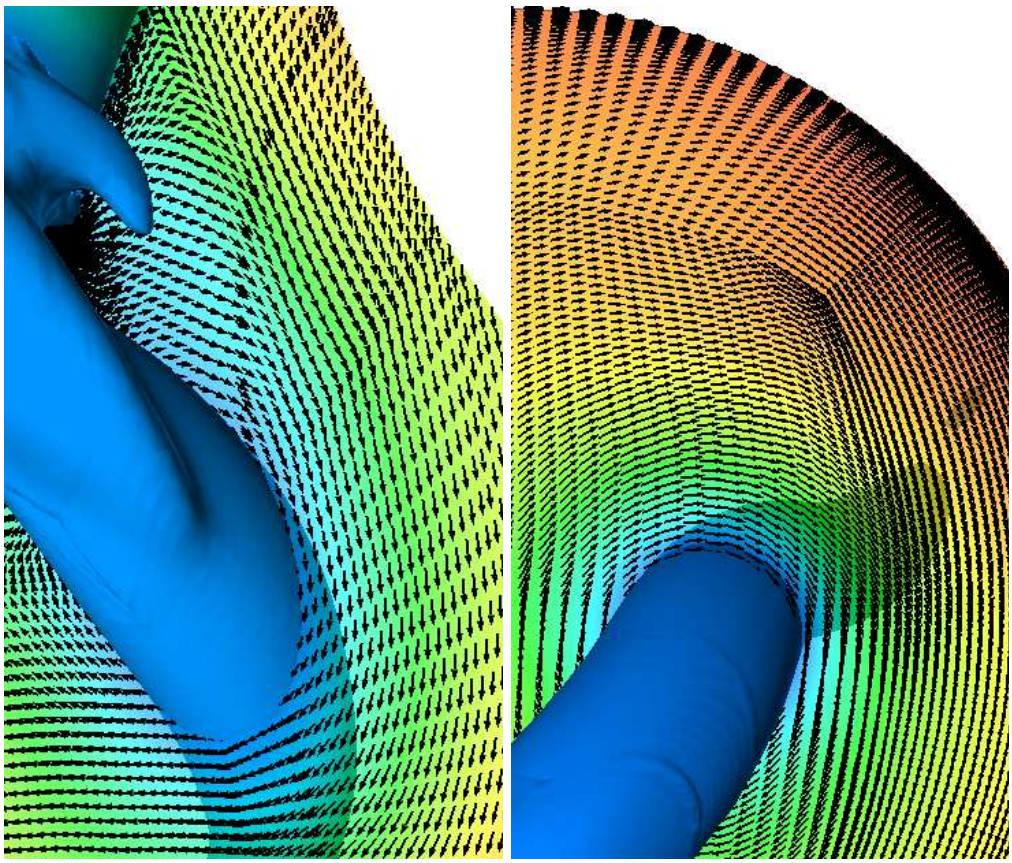

FIGURE 2.4: Snapshot of a precessing vortex core in a draft tube, visualized by an iso-surface of static pressure and velocity vectors in a vertical (left) and horizontal plane (right). The horizontal plane is located approximately one inlet diameter downstream of the runner. The blue colour corresponds to regions of low pressure. The simulation was made at part load conditions, $Q/Q_{opt} = 0.71$. The tilting of the symmetric inlet vortex induces a rotating separated flow region at the runner hub and the reversed flow near the geometrical symmetry axis of the draft tube.

in the vortex core. Figure 2.4 shows that the tilting of the vortex is connected to the separated flow that rotates around the runner hub, and the reversed flow along the geometrical symmetry axis of the draft tube cone, visible in Fig. 2.5.

The conservation of angular momentum and the connection to the increasing swirl level

There are several conservation laws that must be obeyed in an isolated physical system like a draft tube, e.g. the conservation of mass and angular momentum. The axial flux of angular momentum for a steady

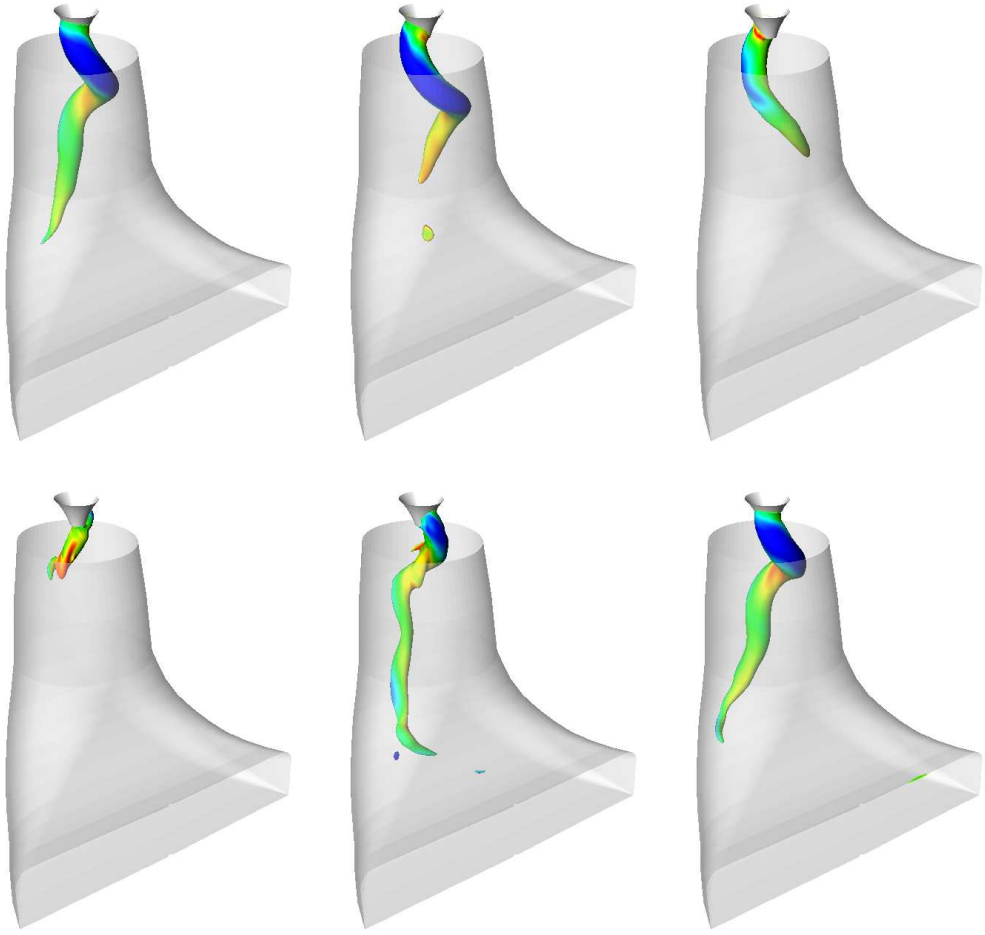

FIGURE 2.5: Row-wise from top: Six snapshots of a precessing vortex core in a draft tube operating at part load, visualized by an iso-surface of the static pressure. The colours represent the vertical velocity, where red corresponds to reversed flow.

flow, in the absence of body forces and shaft work, reads [8]

$$M(z) = \int_A \rho r V_\theta V_z \, dA, \tag{2.8}$$

where A denotes the cross-sectional area of the draft tube and V_θ and V_z are the tangential and axial velocity components, respectively. If the influence of wall friction is negligible, the angular momentum flux must be conserved at each cross-section of the draft tube. Consider, for instance, the evolution of a q vortex in a cylindrical (r, θ, z) coordinate system. The q vortex is defined by the velocity profiles

$$V_z = V_{z,0} + V_{z,1} e^{-r^2/R_c^2}, \tag{2.9}$$

$$V_\theta = \Omega R_c^2 (1 - e^{-r^2/R_c})/r, \tag{2.10}$$

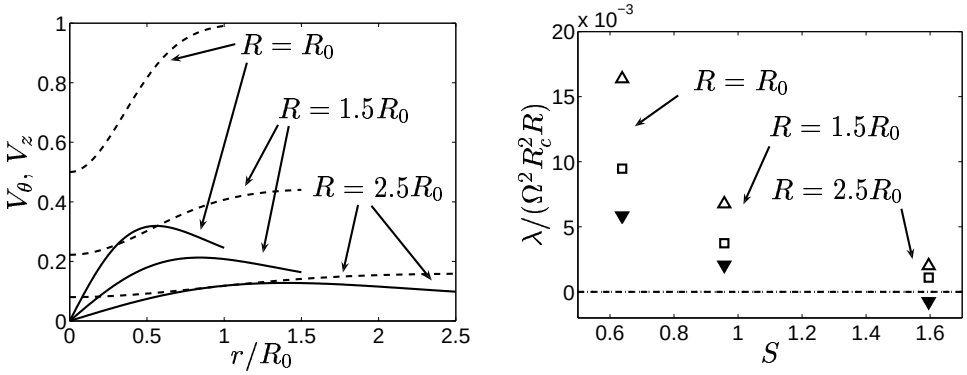

FIGURE 2.6: Left: Three q vortices having identical mass flow and angular momentum, but different radiuses, R. [−−]: Axial velocity. [−]: Tangential velocity. Clearly, the relative swirl level increases with an increase in radius. Right: The three smallest eigenvalues of matrix A, computed for each of the three vortices shown to the left, as a function of the swirl level, $S = \max\{V_\theta\}/V_z(r = 0)$. The smallest eigenvalue (▼) of each vortex will become zero at a certain radius. At this point, the flow will undergo vortex breakdown.

where Ω is the angular velocity of the vortex core. The coefficients R_c, $V_{z,0}$ and $V_{z,1}$ are used to further define the shape of the vortex. Figure 2.6 (left) shows three different q vortices that have identical angular momentum and mass flow, but different radiuses, R. The vortex marked by $R = R_0$ is defined by the coefficients $V_{z,0} = 1$, $\Omega = 1$, $R_c = R/2$ and $V_{z,1} = -0.5/V_{z,0}$. The ratio R_c/R is kept constant at the larger radiuses, but $v_{z,0}$, Ω and, indirectly, $v_{z,1}$, are adjusted to preserve the angular momentum and mass flow. The three sets of velocity profiles may be thought of as representing the flow at three different axial positions in a draft tube, where the vortex having the largest radius corresponds to the flow at the furthest downstream position. Obviously, both the axial and tangential velocity will decrease as the radius increases. However, the swirl level, which may be defined as $S = \max\{V_\theta\}/V_z(r = 0)$, *increases* with an increase in cross-sectional area. The larger the half opening angle of the draft tube (see Fig. 2.1) the faster the increase in swirl level — as long as the flow does not separate from the draft tube walls. An increase in the swirl level of any vortex will eventually force it towards vortex breakdown, see Benjamin [9] or Wang and Rusak [10]. The critical swirl level of an arbitrary quasi-cylindrical vortex can be found using the method of Gyllenram et al. [11] (Paper I). Without going into too much details about the method, it is shown that an equation for the radial velocity component, V_r, of a quasi-cylindrical vortex flow can be written as $A\,V_r = b$,

and that the critical swirl level corresponds to the first singularity of the matrix A. Matrix A is a function of the axial and tangential velocity profiles, and the radius, only. Figure. 2.6 (right) shows the three smallest eigenvalues of matrix A computed for each of the three sets of q vortex profiles shown in Fig. 2.6 (left). As the radius and the swirl level of the vortex increase, the smallest eigenvalue decreases. At a certain point the smallest eigenvalue is zero and thus the matrix is singular, i.e. there exists no quasi-cylindrical flow. For this special q vortex, the singularity is reached at $R < 2.5R_0$, at a critical swirl level of $S = \max\{V_\theta\}/V_z(r=0) \approx 1.4$. However, as the draft tube vortex is also destabilized by the non-uniform adverse pressure gradient, induced by the decreasing tangential velocities (see the next section) and the draft tube elbow, it can be expected to break down much earlier. Furthermore, following the theory of Benjamin [9] (see also Appendix C), the effects of a vortex breakdown will always propagate upstream. Hence, a vortex breakdown that occurs far downstream of the runner may result in a rotating vortex core that propagates upstream until it reaches the inlet.

The decay of tangential velocity and the connection to the adverse pressure gradient

The conservation of angular momentum causes the tangential velocity to decrease as the water flows through the draft tube. This will in turn have an effect on the adverse pressure gradient. The radial momentum equation [12, 13] under the assumptions of axisymmetry and negligible radial velocities (radial equilibrium), can be reduced to

$$\rho V_\theta^2/r = \partial_r P. \tag{2.11}$$

A radial integration of Eq. (2.11) yields

$$P(r,z) - P_{cl}(z) = \rho \int_0^r V_\theta^2/\hat{r}\, d\hat{r}, \tag{2.12}$$

where P_{cl} denotes the pressure at the centerline ($r = 0$). By taking the axial gradient of Equation (2.12) we obtain the pressure gradient at the axis of symmetry, i.e.

$$d_z P_{cl}(z) = \partial_z P(r,z) - \underbrace{\partial_z \int_0^r \rho V_\theta^2/\hat{r}\, d\hat{r}}_{\leqslant 0}. \tag{2.13}$$

Because the tangential velocities decrease in the axial direction, the adverse pressure gradient at the draft tube centerline must be larger

than the adverse pressure gradient elsewhere, i.e. $d_z P_{cl}(z) \geqslant \partial_z P(r,z)$. Following the analysis by Hall [14], an estimation can be made of the difference between the adverse pressure gradients at $r = 0$ and $r = R_c$, where R_c is the radius of the vortex core. Assuming that the axial gradients of the flow are inversely proportional to an axial length scale, $\partial_z \sim L^{-1}$, and noting that the tangential velocity of the vortex core can be approximated by a solid body rotation, $V_\theta = \Omega(z)r$, we get

$$d_z P_{cl}(z) - d_z P(r,z)|_{r=R_c} \sim \rho \xi \Omega^2 R_c, \tag{2.14}$$

where $\xi = R_c/L \sim V_r/V_z$ denotes the order of magnitude of the divergence of the flow. Equation (2.14) indicates that the flow at the centerline will decelerate faster than the surrounding flow, as also noted by Hall [14]. The difference between the adverse pressure gradients increases with the angular velocity, Ω, and the divergence of the flow, ξ. It is likely that this is the main physical mechanism behind the tilting of the initially symmetric vortex. The tilting of the vortex includes both flow reversal near the geometrical centerline and an onset of asymmetry.

2.2.2 The need for accurate simulation methods

The swirling flow in a draft tube of a hydro turbine that operates at part load conditions shows a high degree of complexity. The worst hydrodynamical problems occur when the vortex has reached its critical swirl level, i.e. after the vortex breakdown. A vortex that exits the runner at a swirl level lower than critical may reach its critical swirl level further downstream in the draft tube, as shown in Section 2.2.1. As mentioned in Chapter 2, the efficiency of the draft tube is proportional to the difference between the squares of the inlet and outlet velocities, see Eq. (2.7). The difference grows with the ratio of the inlet and outlet areas. The larger an area ratio, however, the higher the increase in swirl level at part load condition. Consequently, the risk of vortex breakdown increases as well.

A draft tube optimized at the design flow rate may be sensitive to vortex breakdown at part load. The vortex breakdown induces a periodic pressure load, which increases the risk of fatigue failure. In addition, the rotational frequency of a precessing vortex core may be in resonance with the hydraulic circuit of the power plant [15]. There is thus a need for accurate simulation tools to predict the stable operating range of the draft tube, and the frequency and magnitude of the unsteady loads on the machine that follow from a vortex breakdown. The following chapter will discuss the equations governing fluid motion and how the equations are solved, i.e. how the flow can be simulated.

Chapter 3

CFD and Turbulence Modelling

A fluid flow is governed by the Navier-Stokes equations, see Appendix A. Analytical solutions to these equations can be found only for very simple flows. However, by replacing the continuous (unknown) vector function $u_i(x_i, t)$ with its discrete counterpart, a finite set of algebraic equations can be solved numerically in a time stepping procedure. The distance between the points at which the equations are discretized must be very small to be able to obtain a fair approximation of the unknown continous function. The number of discrete points determines how many algebraic equations need to be solved in each time step, and the set of discrete points is usually referred to as the computational mesh, or grid.

If the Reynolds number, $Re = \rho U \Lambda / \mu$, of the flow is known, it is possible to make an *a priori* estimate of how close the discrete points of the computational grid need to be. The characteristic flow data used in the definition of the Reynolds number are the velocity scale, U, the length scale of the largest flow structures, Λ, and the viscosity and density of the fluid, μ and ρ. It can be shown that the ratio of the largest to the smallest length scales of the flow grows as $\Lambda/\lambda \sim Re^{3/4}$, where λ denotes the smallest length scale, see e.g. Barenblatt et al. [16]. In a hydro turbine draft tube flow, the Reynolds number is usually very large, often $Re \gtrsim 10^7$. For this type of flow, the ratio $\Lambda/\lambda \gtrsim 180,000$. The largest length scale in a draft tube flow can be approximated by e.g. the inlet diameter, D. Consequently, the ratio between the largest and the smallest scales of the computational grid should be $D/\Delta \sim \Lambda/\lambda$, where Δ is the smallest distance between two grid points. It follows that $\Delta \lesssim 1/180,000 \sim 10^{-5}$ m for a draft tube flow, if the inlet diameter of the draft tube is, say, $D \sim 1$ m. A direct numerical simulation (DNS) of a draft tube flow using such a fine computational grid is not possible

today. It would require extremely large computational resources.

An alternative approach is to average or filter the governing equations. By averaging or filtering the Navier-Stokes equations, the smallest length scales of the flow need not be computed, and much larger grid spacing can be used. Unfortunately, as shown in Sections 3.2.1 and 3.2.3, this approach gives rise to additional unknowns whose influence on the mean flow has to be approximated by a turbulence model. The larger the fraction of modeled scales of the flow, the lesser is the requirement on grid resolution. The required grid resolution therefore depends on the choice of turbulence model. Most often it is the other way around, i.e. that the resolution or computational time is the limiting factor and determines which approach to turbulence modelling is most suitable for a specific case. There is thus a wide spectrum of complexity of turbulence models. It should be borne in mind, however, that because a turbulence model is merely a *model*, it has a limited range of applicablility and will always cause modelling errors of some magnitude.

3.1 Approaches to flow simulation

Figure 3.1 relates the accuracy of different approaches to flow simulation to the required computional time. The fastest and least accurate methods are steady RANS (Reynolds Averaged Navier-Stokes) simulations. Because they are based on solving the time-averaged Navier-Stokes equations, the solution will not contain any information about the unsteadiness of the flow. Instead, the turbulence model must predict the influence of all unsteady motion on the mean flow. Steady RANS simulations thus require advanced turbulence models. In unsteady RANS simulations, however, there is a potential in resolving the most important unsteady motion. The requirements on grid resolution are approximately the same as for steady RANS simulations, but the simulation time is considerably longer because of the additional time dimension. Skipping to the upper right corner of Fig. 3.1, we find the most accurate method, DNS. Unfortunately, this approach is not yet applicable for industrial purposes, as already concluded in the previous section. Large Eddy Simulation (LES) is the second most accurate method in Fig. 3.1. It has been shown to be a very useful tool when detailed information about the unsteady motions of the flow is necessary. LES requires much finer grid resolution than unsteady RANS. In addition, the time steps must correspond to the time scale of the smallest resolved scales, which is very short. LES is becoming increasingly popular for industrial applications. However, the method is not yet ap-

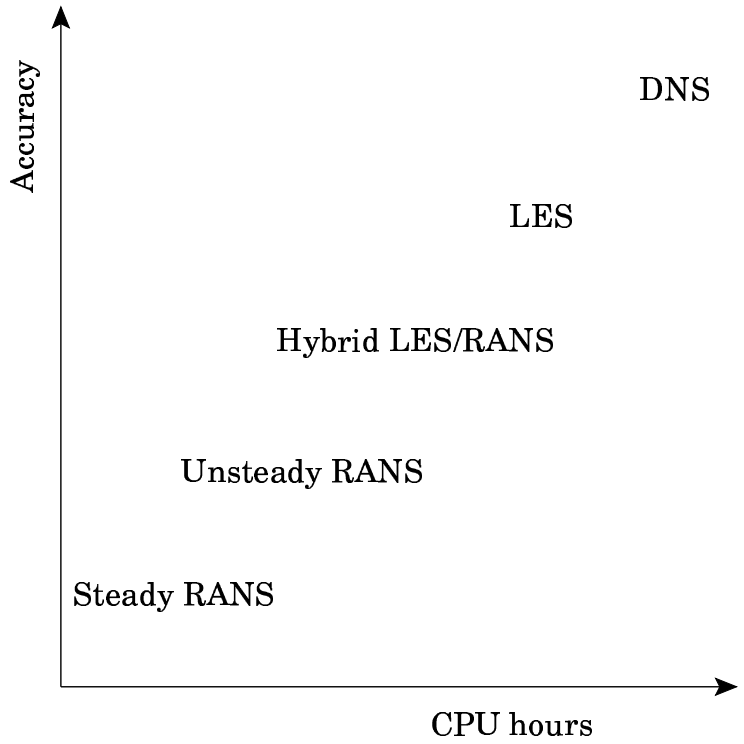

FIGURE 3.1: Qualitative sketch of the accuracy of different approaches to flow simulation as a function of the required computational time.

plicable for high Reynolds number hydro turbine flows unless the effect of the small-scale near-wall turbulence can be accurately modeled by a wall function approach, see Appendix B.3.3.

The only remaining approach is the class of Hybrid LES/RANS methods. The requirements on grid resolution are not much higher than for unsteady RANS. However, because the modeled turbulent length scale is — at least in some regions of the flow — determined by the grid resolution, the time step must not be larger than the time scale that corresponds to such a length scale. This constraint usually requires much shorter time steps than can be used in unsteady RANS, and in the same order of magnitude as LES. The author expects the hybrid LES/RANS methods soon to replace the steady and unsteady RANS simulations as the basic engineering tool. Hence, the numerical work in this thesis is based on the hybrid LES/RANS approach.

3.2 The RANS and LES equations

Because it is time-consuming and expensive to numerically resolve all scales of motion in high Reynolds number flows, the governing equa-

tions are usually averaged or filtered, and the unknowns sought for are the averaged/filtered velocity and pressure field. Unfortunately, any averaging or filtering procedure of non-linear equations gives rise to additional unknowns that must be modelled. In the case of the Navier-Stokes equations, the additional unknowns turn out to be correlations of fluctuating velocities. The unknowns originate from the non-linear convection terms and must accordingly be regarded as turbulent momentum flux. However, they are usually referred to as the Reynolds stress components because they are parts of a second-order tensor. This chapter discusses the differences and similarities between the Reynolds Averaged Navier-Stokes (RANS) equations and the filtered (LES) equations.

3.2.1 The RANS equations

The RANS equations are based on Reynolds decomposition, which reads

$$\Phi_i = \overline{\Phi}_i + \Phi_i', \tag{3.1}$$

where $\overline{\Phi}_i$ is an ensemble-averaged quantity and Φ_i' is a fluctuation from the ensemble average. The ensemble average can be expressed as

$$\overline{\Phi}_i = \lim_{N\to\infty} \frac{1}{N} \sum_{i=1}^{N} \Phi_i, \tag{3.2}$$

where Φ_i is an arbitrary realization and N is the (infinite) number of realizations. The ensemble average is a tool that separates stochastic turbulent fluctuations from the resolved flow. The ensemble average of a stochastic fluctuation equals zero by definition, i.e. $\overline{\Phi}_i' \equiv 0$. Hence, $\overline{\overline{\Phi}}_i = \overline{\Phi}_i$. The basic equations for both applied CFD and theoretical research have been the Reynolds Averaged Navier-Stokes (RANS) equations. The RANS equations can be derived by replacing the arbitrary quantity Φ_i in the Reynolds decomposition, Eq. (3.1), by velocity and pressure, and inserting the decomposed variables in Eq. (A.8), which yields

$$\partial_0(\rho\overline{u}_i) + \partial_j(\rho\overline{u}_i\overline{u}_j) = -\partial_i\overline{p} + \partial_j(\mu(\partial_j\overline{u}_i + \partial_i\overline{u}_j) - \tau_{ij}), \tag{3.3}$$

where the unknown function, $\overline{u}_i$, is the resolved velocity field. The Reynolds stress tensor, $\tau_{ij} = \rho\overline{u_i'u_j'}$, introduces six unknown quantities which must be modeled in order to close the system of equations.

The ensemble average is a concept that implicitely assumes the fluctuations from the mean to be stochastic. However, there is no mathematical way to *a priori* distinguish between deterministic and stochastic scales of an arbitrary flow field, i.e. to distinguish between large

scale unsteadiness of the mean flow and turbulence. Indeed, anything that is resolved in a numerical simulation must be deterministic, per definition. Although it is not yet mathematically proven that there actually exist deterministic and smooth solutions to the incompressible Navier-Stokes equations[1] the author expects repeated DNS simulations to give identical results. In the DNS limit there is consequently no stochastic part of turbulence whatsoever. The stochastic part of the flow must thus be derived from small perturbations of the initial or boundary conditions, to each of the infinite number of flow realizations used in the definition of the ensemble average. The perturbations may be damped out or grow, depending on the flow.

3.2.2 The Boussinesq assumption

It was shown in Section 3.2.1 that the averaging procedure gives rise to six unknown quantities that must be modelled. The simplest and most frequently used turbulence models are based on the Boussinesq assumption, which states that the effect of the small turbulent scales on the resolved flow is dominated by a mixing (diffusion) process. In addition, the small scale turbulent diffusion is assumed to be a linear function of the resolved strain rate, much as the viscous stress of a Newtonian flow is a linear function of the same quantity. The Boussinesq assumption introduces the concept of eddy-viscosity, μ_t, and is mathematically expressed as

$$\partial_j(\mu(\partial_j\overline{u}_i + \partial_i\overline{u}_j) - \tau_{ij}) = \partial_j((\mu + \mu_t)(\partial_j\overline{u}_i + \partial_i\overline{u}_j)). \tag{3.4}$$

The left hand side of this equation is identical to the last term of Eq. (3.3). An identification of terms leads to

$$-\tau_{ij}/\rho = \nu_t(\partial_j\overline{u}_i + \partial_i\overline{u}_j) - 2k\delta_{ij}/3, \tag{3.5}$$

where $\nu_t = \mu_t/\rho$ is the kinematic eddy-viscosity and $k = \overline{u_i'u_i'}/2$ is the turbulent kinetic energy. The last term of Eq. (3.5) is added in order to make the expression valid upon contraction of indices. It is clear that the Boussinesq assumption brings about a drastic simplification. The six unknowns of the Reynolds stress tensor are replaced by two, the single scalar functions ν_t and k. The dimensions of these functions are $[\mathcal{L}^2/\mathcal{T}]$ and $[\mathcal{L}^2/\mathcal{T}^2]$, respectively, where $\mathcal{L}$ denotes length and $\mathcal{T}$ denotes time. It can be shown by dimensional analysis that the kinematic eddy-viscosity can be expressed as a function of any two independent scalars whose dimensions include $\mathcal{L}$ and $\mathcal{T}$.

[1] If you prove this, do not forget to collect the $1,000,000$\$ prize at the Clay Mathematics Institute, Cambridge, Massachusetts, USA.

3.2.3 The filtered LES equations

Another way of averaging is to filter the equations. A time filter (floating average) can be defined as

$$\hat{\Phi}_i(x_i,t) = \frac{1}{\delta T}\int_t^{t+\delta T} \Phi_i(x_i,\hat{t})\, d\hat{t} \tag{3.6}$$

and a spatial (3D) box filter frequently used in LES can be expressed as

$$\hat{\Phi}_i(x_i,t) = \frac{1}{\delta V(x_i)}\int_{\delta V(x_i)} \Phi_i(x_i,t)\, dV, \tag{3.7}$$

where $\delta V(x_i)$ is the local cell volume of the computational grid. By applying a filter to each term of the momentum equations, Eq. (A.8), and thereby solving for a smoother unknown than the exact, the LES equations are obtained, i.e.

$$\partial_0(\rho\hat{u}_i) + \partial_j(\rho\hat{u}_i\hat{u}_j) = -\partial_i\hat{p} + \partial_j(\mu(\partial_j\hat{u}_i + \partial_i\hat{u}_j) - \tau_{ij}^{sgs}) \tag{3.8}$$

where the subgrid stress tensor τ_{ij}^{sgs} is defined as

$$\tau_{ij}^{sgs} = \rho(\widehat{u_iu_j} - \hat{u}_i\hat{u}_j). \tag{3.9}$$

The reader may observe that the only difference between the LES equations, Eq. (3.8), and the RANS equations, Eq. (3.3), is the form of the unknown stress tensor. The equations are identical in all other respects.

3.2.4 Eddy-viscosity turbulence models

There are different approaches to getting an estimate of the turbulent length and time scales that are needed in the Boussinesq assumption. In LES subgrid models, the length scale is usually assumed to be proportional to the local grid spacing, while the time scale is assumed proportional to that of the resolved flow. These assumptions lead to an eddy-viscosity of the form

$$\nu_t \sim \Delta^2|S| \tag{3.10}$$

where Δ is proportional to the local grid spacing and $|S| = \sqrt{2S_{ij}S_{ij}}$ is the magnitude of the strain rate tensor, $S_{ij} = (\partial_j\widehat{u}_i + \partial_i\widehat{u}_j)/2$. Because most unsteadiness is resolved in LES, the turbulent mixing and diffusion are determined by the resolved flow and not by the eddy-visosity. The main purpose of the eddy-viscosity is thus to dissipate the turbulent kinetic energy at the subgrid scales. If the grid spacing and resolved time scale are not good measures of the length and time scales

of the non-resolved unsteadiness, estimates of the non-resolved scales must be obtained from a more complex turbulence model. In RANS simulations, the eddy-viscosity is usually assumed to be a function of two scalar quantities obtained from model transport equations, e.g.

$$\nu_t \sim k/\omega, \tag{3.11}$$

where ω is an inverse turbulent time scale, see Appendix B. A large number of eddy-viscosity models have been proposed during the last decades. Many of them originate from the $k-\varepsilon$ model proposed by Jones and Launder [17] in 1972. However, the baseline model for the studies in this thesis has been the Wilcox [18] $k-\omega$ model described in Appendix B. It is a two-equation model, i.e. two transport equations for turbulent scalar quantities are solved, from which the effect of the motion of the unresolved scales on the resolved flow is approximated. In its original form, however, the model is not suitable for unsteady simulations. It has therefore been modified to suit the application of interest, see Gyllenram and Nilsson [19] (Paper II).

3.3 Interpretations of the RANS and LES equations and a note on hybrid methods

As already noted in Sec. 3.2.3, the filtered and ensemble-averaged equations, Eqs. (3.3) and (3.8), are identical with the exception of the form of the unknown stress tensor, τ_{ij} or τ_{ij}^{sgs}. If an eddy viscosity model is used to close any of the systems of equations, there is no mathematical difference whatsoever between the two. Merely a conceptual difference remains. However, from a numerical viewpoint, one needs only to distinguish between resolved and modelled parts of a simulated unsteady flow field. Whether the modeled parts of turbulence originates from small perturbations in the initial or boundary conditions (RANS), or from subgrid scale fluctuations (LES), is of no practical importance — at least not for flows characterized by large scale unsteadiness induced by e.g. geometrical obstacles or vortex breakdown. In any case, as long as an eddy-viscosity model is used, the eddy-viscosity model should ideally predict the effects of the small scale (non-resolved) turbulent momentum flux on the resolved flow field, and not interfere with flow features that have the potential of being resolved in time and space.

For reasons explained in the beginning of this chapter, it is not possible to numerically resolve all unsteady scales of motion. If the computational grid is not fine enough for an LES, the grid scale, Δ, is not

representative of the mean length scale of the non-resolved flow. In addition, the time scale of the resolved flow may not be expected to represent the non-resolved time scale. Consequently, an eddy-viscosity in the form of Eq. (3.10) will not be a proper model. This is often the case in the vicinity of walls. Away from walls, however, the largest fraction of unsteady motion can be numerically resolved on most computational grids. In regions where the flow is dominated by large scale unsteady structures, an LES is often very accurate.

Contrary to the LES, the weak spot in RANS simulations is that the resolved large scale unsteady motions are often damped out by the turbulence model. This happens when the length and time scales predicted by the turbulence model are too large. The near-wall modelling is on the other hand often quite accurate.

Hybrid LES/RANS methods aim at combining the best of LES and RANS turbulence modelling. Because the methods have the potential of resolving the most important unsteadiness, relatively simple turbulence models may be used. The computational grids may be considerably coarser than those designed for LES. The computational cost will thus be much lower.

Chapter 4

Summary of Papers

Paper I

On the failure of the quasi-cylindrical approximation and the connection to vortex breakdown in turbulent swirling flow

Paper I reports an analytical study of turbulent swirling flow in a straight (or slightly diverging) pipe. A quasi-cylindrical approximation of the time-averaged or steady Navier-Stokes equations is analyzed. Under the assumption that the axial and tangential velocity profiles are known, a linear ordinary differential equation in the form of a two-point boundary value problem for the radial velocity component is derived. Besides that the equation renders possible the computation of the radial velocity component, it can also be used to estimate whether a given swirling flow is near its critical level of swirl (vortex breakdown).

It is found that the quasi-cylindrical approximation is singular for certain swirl levels. The singularities give rise to unphysical solutions that violate the assumptions used in the derivation of the approximation. At the point of singularity, i.e. at the critical swirl level, the flow must develop large axial gradients and/or large scale unsteadiness. The paper shows that the singularities of the quasi-cylindrical approximation correspond exactly to the critical level of swirl of inviscid vortices as derived by Benjamin [9] and Rusak et al. [20] using much more complex methods. In addition, it is argued that the method of finding the critical swirl level presented in Paper I is applicable to arbitrary internal vortices, whether they are inviscid, viscous or turbulent. The applicability to viscous vortices is confirmed by Paper III.

It is shown that the singularities of the quasi-cylindrical approximation are independent of viscosity, i.e. that the onset of vortex break-

down is indeed an inviscid phenomenon. However, the critical swirl level is unique for each vortex and is determined by the distributions of axial and tangential velocities. Because the velocity profiles depend on the Reynolds number, viscous effects can generally not be ignored.

Paper II

Design and validation of a scale-adaptive filtering technique for LRN turbulence modelling of unsteady flow

Paper I gives an explanation of why a swirling flow has to develop large axial gradients and undergo vortex breakdown. However, the analysis does not give information about the non-linear dynamics or unsteadiness of swirling flow as it is based on a linearized form of the time-averaged or steady Navier-Stokes equations. The need of detailed information about the dynamics in swirling flow was the main motivation for Paper II, which examines the swirling flow through a sudden expansion at a Reynolds number of $30,000$ using a novel hybrid LES/RANS method.

A fully resolved LES is not applicable for high Reynolds number flows. Unsteady RANS simulations are better candidates for industrial purposes. However, a disadvantage of RANS simulations in combination with the standard two-equation turbulence models is that they do not provide enough information about the unsteadiness of the flow. It is argued in Paper II that this shortcoming derives from the fact that most RANS turbulence models are tuned for steady simulations, in which the effect of all unsteadiness on the time-averaged flow must be modelled. However, in unsteady simulations, most of the unsteady effects can be resolved in time and space. Hence, the model should be limited to only predict the effects of the non-resolved unsteadiness, i.e. the modelled length and time scales must be filtered.

The dynamic filtering procedure of the turbulent length and time scales originally developed by Willems [21] is generalized and employed in the Wilcox [18] $k-\omega$ turbulence model. The filter sets a limit for the influence of the modelled turbulent length and time scales on the resolved flow in order to reduce the damping effect of the turbulence model. By applying the filter to the eddy-viscosity, the diffusion terms of the momentum and turbulent transport equations are directly influenced. In addition, the modelled production term, P_k, (see Eq. (B.7) in Appendix B) of the $k-$equation is computed using the filtered eddy-viscosity. In the Wilcox [18] $k-\omega$ model, P_k is also used in the pro-

duction of the specific dissipation, for which reason this term is also directly influenced by the filtered eddy-viscosity. A slightly different approach is evaluated in Paper IV.

The filtering procedure is found to be crucial to obtaining unsteady solutions for the chosen test case. It is found that a non-filtered unsteady RANS simulation converges to an erroneous and inaccurate steady state solution. However, by activating the filter, solutions that contain detailed information about the flow dynamics are obtained. Furthermore, the time-averaged results of the filtered simulations are in excellent agreement with experimental data.

Paper III

The influence of boundary layers on the critical swirl level and stability of viscous swirling flow

The theoretical results of Paper I were only validated to other theoretical results, which in turn were based on inviscid theory. It was argued, however, that the method was applicable to any vortex, be it inviscid or not. In Paper III, the theoretical results have been confirmed by a numerical stability analysis of two parameterized viscous vortices, i.e. viscous forms of the Burgers and q vortices. Two-dimensional (axisymmetric) numerical simulations of the evolutions of near critical vortices in a slightly constricted pipe were carried out. The small geometrical constriction acts as a perturbation to the flow. It is shown that the evolution of each vortex indeed depends on whether the inlet swirl level is slightly higher or lower than critical, and that small variations of the magnitude of the geometrical perturbation have a significant impact on a near critical flow. The results confirm that a singularity of the quasi-cylindrical approximation indeed corresponds to the critical swirl level. Also presented is a study of the influence of boundary layers on the critical level of swirl. It is shown that the presence of boundary layers influences the critical level of swirl. However, the critical swirl level is only weakly dependent on the boundary layer thickness.

Paper IV

Assessment of a hybrid LES / RANS turbulence model in unsteady swirling flow

The main motivation in Paper IV was to validate the resolved unsteadiness obtained from using the the filtering method described in Paper II. To further demonstrate the applicability of the hybrid LES/RANS method, the filter is implemented via a user defined function (udf) in the commercial CFD code Fluent, version 6.3, and applied to the $k-\omega$ SST turbulence model. The udf source code is included in Appendix E. In this paper, the filter function influences the turbulent transport equations in a slightly different way than in Paper II. In the $k-\omega$ SST model of Fluent, the production of ω is defined as $P_\omega = \gamma P_k/\nu_t$, where P_k is defined as in Eq. (B.7), see Appendix B. This is also the form proposed by Menter [22]. However, the main consequence of this implementation is that the eddy-viscosity cancels out in the production of ω, P_ω. Hence, the production of ω in its transport equation is not directly influenced by the filter. Despite this difference, the results are very similar to the results of Paper I. Whether there is an advantage of one of the implementations over the other is yet to be determined.

Two test cases were considered, a swirling flow through a sudden expansion at a Reynolds number of $Re = 30,000$, and a flow through the draft tube of a model Francis hydro turbine operating at part load ($Re = 1,476,000$). Measurements of the first mentioned test case serve to validate the time-averaged velocity profiles and resolved normal Reynolds stresses. The simulated frequencies of the flow are validated by transient wall-pressure measurements in the draft tube flow. In addition to the validation by experimental data, the performance of the filtered $k-\omega$ SST model is compared to that of a few alternative turbulence models. It is shown that the novel filtered version of the model surpasses the standard SST model [22, 23], the SST-DES model [22] and the Spalart-Allmaras DES model [24] in accuracy and applicability. The results of another simulation of the draft tube flow, using a Reynolds stress model on a coarser grid, are also used for validation. This simulation was carried out by Stein [25].

In the low Reynolds number sudden expansion test case, the simulation using the standard SST model converges to a steady state solution, as in the case when the Wilcox $k-\omega$ model [18] was used in an earlier Paper II. Surprisingly, the simulation using the SST-DES model also converges to steady state. The Spalart-Allmaras DES model allows unsteady solutions but is found to be extremely sensitive to the

grid resolution. The simulations using the novel filtered version of the SST model, however, show only weak grid dependence, and the time-averaged results agree very well with experimental data.

The high Reynolds number of the draft tube flow allows the use of a wall function approach based on the log-law. The wall function approach is thus used in all draft tube flow simulations. The SST-DES model performs much better in this flow. The resolved frequencies of the simulation agree very well with the measured data. However, the unsteady solutions are similar to those obtained using the dynamic Smagorinsky model, which does the same job in less computational time. The results obtained using the filtered SST model agree equally well with the experimental data and closely resemble the results of Stein [25].

The novel filtered version of the SST model is shown to be a versatile and accurate turbulence model for swirling and recirculating flow against an opposing pressure gradient. It is more accurate and less sensitive to the Reynolds number than the standard SST and the SST-DES models. Furthermore, it is less grid sensitive than the Spalart-Allmaras DES model and gives accurate time-averaged and unsteady results.

Bibliography

[1] P. M. Fearnside. Greenhouse gas emissions from a hydroelectric reservoir (Brasil's Tucuruí dam) and the energy policy implications. *Water, Air and Soil Pollution*, 133:69–96, 2002.

[2] D. Böhme and W. Dürrschmidt (Eds.). *Renewable energy sources in figures — national and international development*. Environmental policy series. Federal Ministry for the Environment, Nature Conservation and Nuclear Safety, Berlin, Germany, 2007.

[3] *Investeringar i elproduktion*, Eskilstuna, Sweden, 2005. Statens Energimyndighet. ER 2005:34, ISSN 1403-1892.

[4] G. Krivchenko. *Hydraulic Machines: Turbines and Pumps, 2nd Ed.* CRC Press, London, UK, 1994.

[5] S. Mauri, J.-L. Kueny, and F. Avellan. Werlé-Legendre separation in a hydraulic machine draft tube. In *Proceedings of the ASME Fluids Engineering Division Summer Meeting*, volume FEDSM2002-31196, Montreal, Quebec, Canada, June 2002.

[6] T. Sarpkaya. On stationary and travelling vortex breakdown. *J. Fluid Mech.*, 45:545–559, 1971.

[7] T.W. Mattner, P.N. Joubert, and M.S. Chong. Vortical flow. Part 1. Flow through a constant diameter pipe. *J. Fluid Mech.*, 463:259–291, 2002.

[8] H. Nilsson. *Numerical Investigations of Turbulent Flow in Water Turbines*. Thesis for the degree of Doctor of Philosophy, ISBN 91-7291-187-5, Chalmers University of Technology, Göteborg, Sweden, 2002.

[9] T. B. Benjamin. Theory of the vortex breakdown phenomenon. *J. Fluid Mech.*, 12:593–629, 1962.

[10] S. Wang and Z. Rusak. The dynamics of a swirling flow in a pipe and transition to axisymmetric vortex breakdown. *J. Fluid Mech.*, 340:177–223, 1997.

[11] W. Gyllenram, H. Nilsson, and L. Davidson. On the failure of the quasi-cylindrical assumption and the connection to vortex breakdown in turbulent swirling flow. *Phys. Fluids*, 19:4, 2007.

[12] G.K. Batchelor. *Introduction to Fluid Dynamics*. Cambridge Mathematical Library, Cambridge, 1967.

[13] R. L. Panton. *Incompressible Flow*. John Wiley & Sons, Inc, New York, USA, 1996.

[14] M.G. Hall. Vortex breakdown. *Ann. Rev. Fluid Mech.*, 4:189–218, 1972.

[15] C. Nicolet, J.-J. Herou, B. Greiveldinger, P. Allenbach, J.-J. Simond, and F. Avellan. Methodology for Risk Assessment of Part Load Resonance in Francis Turbine Power Plant. In *IAHR Int. Meeting of WG on Cavitation and Dynamic Problems in Hydraulic Machinery and Systems*, Barcelona, Spain, 2006.

[16] G. I. Barenblatt, A. J. Chorin, and V. M. Prostokishin. Comment on the paper 'On the scaling of three-dimensional homogeneous and isotropic turbulence' by Benzi et al. *Physica D: Nonlinear phenomena*, 127(1-2):105–110, 1999.

[17] W. P. Jones and B. E. Launder. The prediction of laminarization with a two-equation model of turbulence. *Int. J. Heat and Mass Transfer*, 15:301–314, 1972.

[18] D.C. Wilcox. Reassessment of the scale-determining equation for advanced turbulence models. *AIAA J.*, 26(11):1299–1310, 1988.

[19] W. Gyllenram and H. Nilsson. Design and validation of a scale-adaptive filtering technique for lrn turbulence modeling of unsteady flow. *Accepted for publication in J. Fluids Engineering*, 2008.

[20] Z. Rusak, C. H. Whiting, and S. Wang. Axisymmetric breakdown of a q-vortex in a pipe. *AIAA J.*, 36:1848–1853, 1998.

[21] W. Willems. *Numerische Simulation turbulenter Scherströmungen mit einem Zwei-Skalen Turbulenzmodell*. Thesis for the degree of Doctor of Philosophy, Rheinish-Westfälischen Technischen Hochschule, Aachen, Germany, 1996.

[22] F. R. Menter, M. Kuntz, and R. Langtry. Ten years of industrial experience with the SST turbulence model. In *Turbulence, Heat and Mass Transfer*, volume 4. Begell House, Inc., 2003.

[23] F.R. Menter. Two-equation eddy-viscosity turbulence models for engineering applications. *AIAA J.*, 32(8):1598–1605, 1994.

[24] P.R. Spalart, W-H. Jou, M. Strelets, and S.R. Allmaras. Comments on the feasibility of LES for wings, and on a hybrid RANS/LES approach. In *Advances in DNS/LES*, 1st AFOSR Int. Conf. on DNS/LES, Aug. 4-8, Ruston, LA, 1997. C. Liu & Z. Liu (Eds.), Greyden Press, Columbus, OH.

[25] P. Stein. *Numerical Simulation and Investigation of Draft Tube Vortex Flow*. PhD thesis, Coventry University, England, 2007.

[26] D. C. Wilcox. *Turbulence Modeling for CFD*. DCW Industries Inc., La Cañada, CA, USA, 2 edition, 2002.

[27] S. B Pope. *Turbulent Flows*. Cambridge University Press, Cambridge, UK, 2000.

[28] W. Gyllenram and H. Nilsson. Assessment of a hybrid LES/RANS turbulence model in unsteady swirling and recirculating flow. 2008. Submitted to scientific journal.

[29] P.A. Durbin. On the $k - \varepsilon$ stagnation point anomaly. *Int. J. Heat and Fluid Flow*, 17:88–89, 1995.

[30] G. B. Folland. *Fourier Analysis and its Applications*. Wadsworth & Cole, 1992.

[31] J. Jeong and F. Hussain. On the identification of a vortex. *J. Fluid Mech.*, 285:69–94, 1995.

Appendix A

The Navier-Stokes Equations

The formulation of the equations governing fluid motion is ascribed to the French engineer/mathematician C.-L. Navier (1785-1836) and the English mathematician G.G. Stokes (1819-1903). This chapter introduces the Navier-Stokes equations and gives a discussion of a few of the assumptions underlying the equations.

A.1 The continuity equation

The continuity equation is derived from the law of mass conservation, i.e.

$$d_0 m|_V = d_0 \int_V \rho \, dV = 0, \tag{A.1}$$

where $V = V(x_i, t)$ is an arbitrary volume and $\rho = \rho(x_i, t)$ is the density of the fluid. Using the Leibniz theorem, this can be expressed as

$$\int_V \partial_0 \rho \, dV + \int_S \rho u_i n_i \, dS = 0, \tag{A.2}$$

where n_i is the surface normal of the arbitrary volume and $u_i = u_i(x_i, t)$ the velocity vector. The equation states that the change of mass of an arbitrary fluid particle (volume) equals the net flow through its boundaries. The surface integral in Eq. (A.2) can be transformed to a volume integral using the Gauss theorem, which yields

$$\int_V \partial_0 \rho + \partial_i (\rho u_i) \, dV = 0. \tag{A.3}$$

Because the equation must be valid for an arbitrary region, the integrand must be identically zero. By applying the product rule, the integrand of Eq. (A.3) can be written as

$$\partial_0 \rho + u_i \partial_i \rho + \rho \partial_i u_i = 0. \tag{A.4}$$

Now, if the *flow* is considered incompressible, the sum $\partial_0\rho + u_i\partial_i\rho = 0$. Thus, a flow is incompressible if the density of any fluid particle we follow is constant. In this case, the continuity equation simplifies to

$$\partial_i u_i = 0. \tag{A.5}$$

Note that density variations (e.g. stratification because of salinity or temperature gradients) can still exist in an incompressible flow. However, if the *fluid* is considered incompressible and homogeneous, then $\partial_0\rho = u_i\partial_i\rho = 0$, and Eq. (A.5) follows once again. Hence, the flow of an incompressible and homogeneous fluid will always be incompressible, but an incompressible flow does not necessarily have to involve an incompressible and homogeneous fluid.

Generally speaking, the density of a fluid is a function of pressure, i.e. it is governed by thermodynamical laws. A discussion and derivation of the conditions under which a flow of a compressible fluid can be considered incompressible are given in Panton [13]. In short, a flow of any fluid can be considered incompressible if the density is only very weakly dependent on pressure. This is usually true at low enough Mach numbers, $M = |u_i|/u_p$, where u_i and u_p denote the local velocity vector of the flow and the speed of sound (pressure) waves in the fluid, respectively. A commonly used limit is $M < 0.3$. The speed of sound in water is approximately 1500 m/s. The assumption of incompressibility is thus valid at velocities up to 450 m/s.

A.2 The momentum equation

The momentum equation is merely Newton's second law, $m\,\mathbf{a} = \mathbf{F}$, formulated for a fluid particle. The time rate of change of momentum per unit volume can be expanded to

$$\begin{aligned} D_0(\rho u_i) &= \partial_0(\rho u_i) + u_j\partial(\rho u_i) \\ &= \rho\partial_0 u_i + \rho u_j\partial_j u_i + u_i\left(\partial_0\rho + u_j\partial_j\rho\right). \end{aligned} \tag{A.6}$$

The last term vanishes for incompressible flow. The time rate of change of momentum must be balanced by the normal (pressure) and shear forces, per unit volume, acting on the particles' surface. For an incompressible Newtonian flow in a stationary frame of reference, we thus have

$$\rho\partial_0 u_i + \rho u_j\partial_j u_i = -\partial_i p + \partial_j\left(\mu(\partial_j u_i + \partial_i u_j)\right) + \rho g_i. \tag{A.7}$$

The most important property of a Newtonian fluid is that the shear stress, τ_{ij}, acting on a fluid element is a linear function of the strain

rate, i.e. $\tau_{ij} = \mu(\partial_j u_i + \partial_i u_j) = 2\mu S_{ij}$, where S_{ij} is the strain rate tensor. The molecular viscosity, μ, is a function of temperature. The Newtonian assumption is valid for water and air at normal temperatures. Three examples of non-Newtonian fluids are paper pulp, liquid polymers and blood, for which fluid-specific models have to be used for the stress-strain relationship. The gravitational body force, ρg_i, in Eq. (A.7), is only important at free surfaces or in stratified flows, and may be integrated and included in the pressure term, $\partial_j p$. The pressure, p, is in incompressible flow merely regarded as the net normal force acting on a fluid element and should not be confused with the thermodynamic pressure. Neither free surfaces nor stratification or varying molecular viscosity is considered in the present work. Equation (A.7) can thus be expressed as

$$\partial_0(\rho u_i) + \partial_j(\rho u_i u_j) = -\partial_i p + \partial_j \left(\mu(\partial_j u_i + \partial_i u_j)\right). \tag{A.8}$$

Note that the left hand side is now expressed in a conservative form. This is the form usually implemented in CFD software. The molecular viscosity is kept within the brackets to show its relation to the Boussinesq assumption, which is discussed in Section 3.2.2.

A.3 The solution to the equations

The Navier-Stokes equations belong to the class of non-linear partial differential equations. The solution to the equations is the local velocity vector, $u_i(x_i, t)$ and pressure, $p(x_i, t)$. The magnitude of u_i determines the speed of a fluid particle at an instant, and the direction of the vector its current course. Anyone who has observed the apparently chaotic fluid motions in, for instance, the wake behind a boat, realizes that it is not straightforward to find a solution to the Navier-Stokes equations. In the vast majority of applications, one has to settle for an approximate solution.

Appendix B

Wilcox' (1988) $k-\omega$ model

The Wilcox $k-\omega$ model [18] is a two-equation model, i.e. two transport equations for turbulent scalar quantities are solved, from which the effect of the motion of the unresolved scales on the resolved flow is approximated. In this appendix the model and its derivation is briefly discussed, starting from the exact equation for the turbulent kinetic energy.

B.1 The turbulent kinetic energy equation

An exact equation for the turbulent kinetic energy of the non-resolved velocity fluctuations, $k = \overline{u_i' u_i'}/2$, which can be derived from Eqs. (A.8) and (3.3) reads

$$\begin{aligned} \partial_0 k + \overline{u}_j \partial_j k = & -\tau_{ij}\partial_j \overline{u}_i \\ & + \partial_j \left(-\overline{p' u_i}\delta_{ji}/\rho - \overline{u_i' u_i' u_j'}/2 + \nu \partial_j k \right) \\ & - \overline{\partial_j u_i' \partial_j u_i'}. \end{aligned} \tag{B.1}$$

This equation is often written in a condensed form, i.e.

$$\partial_0 k + \overline{u}_j \partial_j k = \mathcal{D}_k + \mathcal{P}_k - \varepsilon \tag{B.2}$$

in which

$$\mathcal{D}_k = \partial_j \left(-\overline{p' u_i}\delta_{ji}/\rho - \overline{u_i' u_i' u_j'}/2 + \nu \partial_j k \right) \tag{B.3}$$

$$\mathcal{P}_k = -\tau_{ij}\partial_j \overline{u}_i \tag{B.4}$$

$$\varepsilon = \nu \overline{\partial_j u_i' \partial_j u_i'}. \tag{B.5}$$

Terms $\mathcal{D}_k$ and $\mathcal{P}_k$ are referred to as the turbulent diffusion and production terms, respectively. The last term, ε, is called the dissipation rate. This is the amount of kinetic energy of the non-resolved flow that is

transformed to the molecular energy of the fluid. A transport equation for ε can also be derived from Eqs. (A.8) and (3.3), see e.g. Wilcox [26]. There is a large number of new unknowns in the exact equation for the turbulent kinetic energy, Eq. (B.1), not to mention the number of new unknowns in the exact ε equation. All of them must be related to the resolved velocity field, or to the quantities k and ε themselves.

B.2 The model equations

The $k-\omega$ model of Wilcox [18] solves the transport equations for the turbulent kinetic energy, k, and the specific dissipation rate, $\omega \sim \varepsilon/k$. There are three terms in Eq. (B.2) that need to be modeled: the turbulent diffusion term, $\mathcal{D}_k$, the production term, $\mathcal{P}_k$, and the dissipation rate, ε. The diffusion term, Eq. (B.3), is modeled by a gradient law,

$$-\overline{p'u_i}\delta_{ji}/\rho - \overline{u_i'u_i'u_j'}/2 = (\nu_t/\sigma_k)\partial_j k, \tag{B.6}$$

which states that k is diffused from regions of high k to regions of lower k. The model constant σ_k is the turbulent Prandtl number, i.e. the ratio between the viscous and turbulent diffusion. The production term, $\mathcal{P}_k$, is modeled using the Boussinesq assumption described in Section 3.2.2, which yields

$$-\tau_{ij}\partial_j\overline{u}_i = 2\nu_t S_{ij}\partial_j\overline{u}_i = P_k, \tag{B.7}$$

where $S_{ij} = (\partial_j\overline{u}_i + \partial_i\overline{u}_j)/2$. The only remaining term to be modelled is now the dissipation rate, ε, i.e. the amount of turbulent kinetic energy that is transferred to the molecular energy of the fluid. By assuming that the energy that is dissipated at the molecular scales can be represented by the energy contained at the modeled scales, the dissipation rate can be estimated from the modelled turbulent length and time scales,

$$\varepsilon = L_t^2/T_t^3. \tag{B.8}$$

Using the relations for the modelled turbulent length and time scales of the $k-\omega$ model, i.e.

$$L_t = \sqrt{k}/(\beta\omega), \tag{B.9}$$
$$T_t = (\beta\omega)^{-1}, \tag{B.10}$$

we get $\varepsilon = \beta\omega k$. The specific dissipation rate, ω, is modeled by means of a separate transport equation. The Wilcox [18] $k-\omega$ model reads

$$\partial_0 k + U_j\partial_j k = \partial_j\left((\nu + \nu_t/\sigma_k)\partial_j k\right) + P_k - \beta\omega k, \tag{B.11}$$
$$\partial_0\omega + U_j\partial_j\omega = \partial_j\left((\nu + \nu_t/\sigma_\omega)\partial_j\omega\right) + \omega(c_{\omega 1}P_k - c_{\omega 2}k\omega)/k, \tag{B.12}$$

where

$$\nu_t = k/\omega, \tag{B.13}$$

and the coefficients of the model are

$$\beta = 0.09,\ c_{\omega 1} = 5/9,\ c_{\omega 2} = 3/40,\ \sigma_k = 2,\ \sigma_\omega = 2. \tag{B.14}$$

One of the chief advantages of the $k-\omega$ model over the $k-\varepsilon$ model is that it can be integrated all the way to the wall without using any damping functions in the inner part of the boundary layer. Hence, it belongs to the class of low Reynolds number (LRN) models. If the boundary layer is not numerically resolved, the use of standard wall functions is still possible, see Sec. B.3.3. Wilcox proposed the $k-\omega$ model according to Eqs. (B.11) and (B.12) in 1988. Since then, the model has been continously developed and modified in order to make it applicable to a wider range of flows. One of the most popular $k-\omega$ models in use today is the $k-\omega$ SST model, derived by Menter [22, 23], which is actually a mix between a $k-\omega$ and a $k-\varepsilon$ model. Without going into detail, it combines the good near-wall behavior of the $k-\omega$ model with the good behavior of the $k-\varepsilon$ model in the outer part of the flow. It is also designed to be applicable in stagnation regions and in flows with strong adverse pressure gradients.

B.3 Wall modelling

The time-averaged incompressible Navier-Stokes equations for fully developed flow between two parallel plates read

$$\partial_x \overline{p} = \partial_y(\mu \partial_y \overline{u} - \rho \overline{u'v'}) \tag{B.15}$$

$$\partial_y \overline{p} = \partial_y(-\rho \overline{v'v'}), \tag{B.16}$$

where u and v denote the streamwise and wall normal velocity components, respectively. It follows from integration of Eq. (B.16) that $\overline{p}(x,y) = -\rho\overline{v'v'} + \overline{p}_w(x)$, where $\overline{p}_w$ is the wall pressure. By differentiating $\overline{p(x,y)}$ with respect to the streamwise coordinate, x, and noting that $\partial_x \rho \overline{v'v'} = 0$, we can write Eq. (B.15)

$$\partial_x \overline{p}_w = \partial_y(\mu \partial_y \overline{u} - \rho \overline{u'v'}) \tag{B.17}$$

which can be integrated to yield

$$\partial_x \overline{p}_w y = \mu \partial_y \overline{u} - \tau_w - \rho \overline{u'v'} \tag{B.18}$$

where the definition of the wall shear stress, $\tau_w \equiv \mu \partial_y \overline{u}|_{y=0}$, has been used. At $y = \delta$, where δ is the half width between the two plates (i.e.

the boundary layer thickness), $\mu\partial_y\overline{u} = \rho\overline{u'v'} = 0$. Hence, $\partial_x\overline{p} = -\tau_w/\delta$, which means that the pressure gradient is balanced by the wall shear stress. It follows that

$$\tau_w(1 - y/\delta) = \mu\partial_y\overline{u} - \rho\overline{u'v'}. \tag{B.19}$$

By multiplying this expression with $(\rho u_\tau^2)^{-1}$, where $u_\tau^2 \equiv \tau_w/\rho$, a non-dimensional form is obtained, i.e.

$$(1 - y^+/Re_t) = \partial_{y^+}u^+ - \overline{u'v'}^+, \tag{B.20}$$

where the definitions $u^+ \equiv \overline{u}/u_\tau$, $y^+ \equiv \rho u_\tau y/\mu$ and $Re_t \equiv \rho u_\tau \delta/\mu$ are used. This equation is exact for fully developed flow between two parallel plates.

B.3.1 The law of the wall

It is clear that, if $\overline{u'v'}^+ \to 0$ as $y^+ \to 0$ in Eq. (B.20), then $\partial_{y^+}u^+ = 1$. In integrated form, this yields the *law of the wall*,

$$u^+ = y^+, \tag{B.21}$$

which states that the velocity profile is linear at small y^+. The linear relation is valid for $y^+ \lesssim 5$, a region usually referred to as the viscous sublayer.

B.3.2 The logarithmic law

A fully developed flow between two parallel plates is completely specified by ρ, μ, δ and u_τ. Following the reasoning of Pope [27], only two independent groups can be formed from these quantities and the wall normal coordinate, y, for instance y/δ and $y^+ = \rho u_\tau y/\mu$. We can therefore express the velocity gradient by using a non-dimensional function, $\Phi(y^+, y/\delta) = \Phi_1(y^+)\Phi_2(y/\delta)$, as

$$\partial_y\overline{u} = u_\tau/y\,\Phi_1(y^+)\Phi_2(y/\delta). \tag{B.22}$$

This can be completely non-dimensionalized by multiplication with $\mu/(\rho u_\tau^2)$,

$$\partial_{y^+}u^+ = 1/y^+\,\Phi_1(y^+)\Phi_2(y/\delta). \tag{B.23}$$

At small y^+, $\Phi(y^+, y/\delta) \sim \Phi_1(y^+)$, and the law of the wall (see Sec B.3.1) may be reconstructed. At larger y^+, on the other hand, $\Phi_1(y^+)$ must approach a constant, while the outer scaling $\Phi_2(y/\delta)$ determines the profile. This constant is referred to as $1/\kappa$, which leads to

$$\partial_{y^+}u^+ = 1/(\kappa y^+). \tag{B.24}$$

The logarithmic law (a.k.a. the *log-law*) is obtained from integration of Eq. (B.25), which gives

$$u^+ = 1/\kappa \, \ln(E\, y^+), \tag{B.25}$$

where $E \approx 9$ and $\kappa \approx 0.4$. The log-law has been shown to be a good approximation of the axial velocity profile at $30 < y^+ < 100$ in a fully developed boundary layer.

B.3.3 Wall functions

Wall functions are used to model the effect of near-wall turbulence in the case that the boundary layer is not fully resolved. They are generally based on the law of the wall or the log-law. In this thesis, wall functions are only used in the simulations of the draft tube flow described in Gyllenram et al. [28]. These simulations were carried out using the Fluent commercial software. In an LES using Fluent, the wall shear stress is obtained from the laminar stress-strain relationship, Eq. (B.21), if the computational grid is considered fine enough to resolve the viscous sublayer, i.e. if $y_1^+ < 3$. In the following, subscript 1 will denote a quantity that is evaluated in the wall-adjacent cell. If the wall-adjacent cell is placed at $y_1^+ > 10$, the law of the wall, Eq. (B.25), using $\kappa = 0.42$ and $E = 9.79$, is employed. If the grid is such that the wall-adjacent cell falls within the buffer region ($3 \leqslant y^+ \leqslant 10$), then the two above laws are blended. In any case, the friction velocity, u_τ, is iteratively determined.

Fluent uses nearly the same wall function approach as above for DES and RANS simulations based on the $k-\omega$ SST turbulence model. However, the friction velocity, u_τ, and non-dimensional wall distance, y^+, in Eqs. (B.21) and (B.25), are replaced by

$$u^* \equiv \frac{\overline{u}_1 \beta^{1/4} k_1^{1/2}}{\tau_w/\rho} \tag{B.26}$$

and

$$y^* \equiv \frac{\rho \beta^{1/4} k_P^{1/2} y_1}{\mu}, \tag{B.27}$$

respectively. Using the default Fluent settings, the switch between the law of the wall, Eq. (B.21), and the log law, Eq. (B.25), is at $y^* = 11.225$.

B.3.4 Boundary conditions for turbulent quantities

If the boundary layer is fully resolved, the boundary conditions for k and ω at hydraulically smooth walls read

$$k = 0 \tag{B.28}$$

$$\omega = 6\nu/(c_{\omega 2} y^2), \tag{B.29}$$

where the latter condition is defined at the wall-adjacent cell. If the wall-adjacent cell is within the logarithmic region, Fluent uses the boundary conditions

$$\partial_y k = 0 \tag{B.30}$$

$$\omega = u^*/(\sqrt{\beta}\kappa y), \tag{B.31}$$

for the turbulent kinetic energy and specific dissipation, respectively. In addition, the production of turbulent kinetic energy, Eq. (B.7), is in the wall-adjacent cell evaluated as

$$P_k = u^{*4}/(\sqrt{k}y). \tag{B.32}$$

B.4 The realizability constraint

The realizability constraint derived by Durbin [29] was used in Paper II. The constraint is needed in any eddy-viscosity formulation in order to avoid negative turbulent normal stresses. If the inequality

$$\overline{u_\gamma'^2} \geqslant 0 \tag{B.33}$$

is inserted in the Boussinesq assumption, Eq. (3.5), and the coordinate system is rotated until the strain rate tensor, S_{ij}, becomes strictly diagonal, Eq. (3.5) can be rewritten as

$$0 \leqslant -2\nu_t \lambda_\gamma + \frac{2}{3}k. \tag{B.34}$$

Here, λ_γ is an eigenvalue of S_{ij} and $\gamma = 1, 2$ or 3. By solving the characteristic equation for λ_γ, it follows that

$$|\lambda_\gamma| \leqslant \sqrt{2S_{ij}S_{ij}/3}. \tag{B.35}$$

After inserting this expression into Eq. (B.34) it can be shown that the eddy-viscosity of the $k-\omega$ model must be limited, i.e.

$$\nu_t = \min\{k/\omega,\, k/\sqrt{6S_{ij}S_{ij}}\}. \tag{B.36}$$

The realizability constraint becomes especially important in regions of large normal strains (e.g. stagnation points) where two-equation models usually tend to overpredict the production of turbulence.

Appendix C

Basic Principles of Inviscid Vortex Breakdown

Two of the papers upon which this thesis is based discuss vortex breakdown from a theoretical point of view. The concept of super- and subcritical states of a vortex is frequently used in these papers, as well as in many other papers that discuss vortex breakdown. A note and discussion about the origin of this concept are therefore appropriate.

One of the landmark papers on vortex breakdown was written by Benjamin [9] in 1962. Benjamin introduced the concept of sub- and supercritical states of the flow field by analogy with the hydraulic jump, i.e. that the flow suddenly switches between two conjugate states at some critical level. Benjamin's theory is based on a perturbation analysis of the Squire-Long equation. The equation for a perturbation of a given flow field is derived. By introducing analytical perturbations to the flow, an eigenvalue problem is obtained. Benjamin showed that the sign of the smallest eigenvalue determines whether or not a perturbation to the flow can be sustained. First some fundamental inviscid flow theory is in place, however.

C.1 Inviscid flow

The equations describing the motion of an incompressible, inviscid fluid are the Euler equation and the continuity equation, i.e.

$$D_0\mathbf{u} = \mathbf{g} - \nabla p/\rho, \tag{C.1}$$

and

$$\nabla \cdot \mathbf{u} = 0, \tag{C.2}$$

where $\mathbf{u}$ is the velocity vector. The definition of the vorticity vector, $\omega = \nabla \times \mathbf{u}$, together with a basic vector identity gives

$$\nabla(\mathbf{u} \cdot \mathbf{u})/2 \equiv \mathbf{u} \cdot \nabla \mathbf{u} + \mathbf{u} \times \omega. \tag{C.3}$$

Inserting this in the steady version of equation (C.1) leads to

$$\mathbf{u} \times \omega = \nabla(u^2/2 + p/\rho - \mathbf{g} \cdot \mathbf{x}) = \nabla H \tag{C.4}$$

where H is the total head and $u^2 = \mathbf{u} \cdot \mathbf{u}$. The gravity term will from now on be incorporated in the pressure term. Using another vector property,

$$\mathbf{a} \cdot (\mathbf{a} \times \mathbf{b}) \equiv \mathbf{0}, \tag{C.5}$$

shows that the total head, H, is constant along velocity or vorticity vectors since, in general,

$$\mathbf{u} \cdot \nabla H = 0 \tag{C.6}$$

$$\omega \cdot \nabla H = 0. \tag{C.7}$$

The orthogonality of ∇H and $\mathbf{u}$ is essentially the *Bernoulli theorem*, i.e. the total head is constant along a streamline. An important aspect of the above is that, in steady axisymmetric flow, the vorticity lines must lie in a stream surface.

C.2 The Squire-Long equation

Consider a steady, incompressible inviscid and axisymmetric swirling flow in a cylinder, in which (r, θ, z) denote the radial, tangential and axial directions, respectively, and u, v, w are the corresponding velocities. Subscripts denote spatial derivatives. The equation for the stream function in this flow is the Squire-Long equation, which can be derived from the Navier-Stokes equation. It reads

$$H'(\psi) - (2y)^{-1} I'(\psi) = \psi_{yy} + (2y)^{-1} \psi_{zz}, \tag{C.8}$$

where the variable $y = r^2/2$ and the functionals $H(\psi) = q^2/2 + p/\rho$ and $I = K(\psi)^2/2 = (rv)^2/2$ describe the total head and the swirl, respectively. The physical interpretation of the stream function is that lines of constant ψ describe fluid particle paths. Another interpretation is that $\psi(a) - \psi(0) = Q$ is the volume flow rate through a cross-section of radius a. Function ψ may arbitrarily be set to zero at the cylinder axis. The velocities can be reconstructed from the stream function by the relations

$$u = -r^{-1}\psi_z, \; w = r^{-1}\psi_r. \tag{C.9}$$

The stream function satisfies identically the continuity equation for this flow. For a detailed derivation of the Squire-Long equation, see Benjamin [9]. Assume we have a primary unperturbed swirling flow in a cylinder of radius a. The tangential and axial velocities are $v = V(y)$ and $w = W(y)$, respectively, and the radial velocity component is zero. The superposition of a small steady perturbation and a stream function, Ψ, can thus be written

$$\psi(y,z) = \Psi(y) + \epsilon\tilde{\psi}(y,z), \tag{C.10}$$

where the stream function, Ψ, is a solution to equation (C.8). To a first-order approximation in ϵ, the Squire-Long equation for the perturbation can be written

$$\tilde{\psi}_{yy} + (2y)^{-1}\tilde{\psi}_{zz} - (H''(\Psi) - (2y)^{-1}I''(\Psi))\tilde{\psi} = 0. \tag{C.11}$$

Noting that the coefficients of $\tilde{\psi}$ are functions of the unperturbed stream function $\Psi(y)$ only, they can after some rearranging be expressed as functions of only y. Noting that $W = \Psi_y$ and $V^2 = I/y$,

$$H = \frac{p}{\rho} + \frac{1}{2}W^2 + \frac{1}{2}I/y \tag{C.12}$$

$$\begin{aligned}\frac{dH}{d\Psi} &= \frac{\partial H}{\partial y}\frac{\partial y}{\partial \Psi} = \left(\frac{p_y}{\rho} + WW_y + \frac{1}{2}(I_y/y - I/y^2)\right)\frac{1}{W} \\ &= \frac{p_y}{\rho W} + W_y + \frac{1}{W}(I_y/2y - I/2y^2).\end{aligned} \tag{C.13}$$

In order to obtain an approximation of the pressure field, p, the *radial equilibrium* relation is used. The relation is exact for steady, axisymmetric inviscid flow in which the radial velocities are zero, and reads

$$p_r = \rho V^2/r \Rightarrow p_y = \rho I/2y^2 \tag{C.14}$$

Equation (C.13) can then be reduced to

$$\frac{dH}{d\Psi} = W_y + \frac{1}{2}I_y/yW. \tag{C.15}$$

Since $d/d\Psi = W^{-1}d/dy$, we see that

$$H''(\Psi) = W_{yy}/W + \frac{1}{2}I_{yy}/yW^2 - \frac{1}{2}I_y/y^2W^2 \tag{C.16}$$

$$I''(\Psi) = I_y y/W^2 \tag{C.17}$$

and equation (C.11) simplifies to

$$\tilde{\psi}_{yy} + (2y)^{-1}\tilde{\psi}_{zz} - \left(\frac{W_{yy}}{W} - \frac{I_y}{2y^2W^2}\right)\tilde{\psi} = 0. \tag{C.18}$$

This is a second-order differential equation for the development of perturbations in a steady, incompressible, inviscid and axisymmetric swirling flow in a cylinder. The boundary conditions for the equation are obtained by assuming that the perturbations do not change the volume flow rate, $Q = 2\pi\psi|_{y=a}$. Clearly

$$\tilde{\psi}(0,z) = 0 \tag{C.19}$$
$$\tilde{\psi}(a,z) = 0. \tag{C.20}$$

The boundary conditions in the axial direction are not important at the moment.

C.2.1 Super- and subcritical flow regimes

Introducing the axisymmetric perturbation

$$\tilde{\psi}(y,z) = \phi(y)\exp(\gamma z) \tag{C.21}$$

into equation (C.18) gives a regular Sturm-Liouville eigenvalue problem

$$L(\phi) + \frac{\gamma^2}{2y}\phi = L(\phi) + \lambda m\phi = 0 \tag{C.22}$$

where $\lambda = \gamma^2$ and the operator L is defined as

$$L(\cdot) = \frac{\partial^2}{\partial y^2} + \left(\frac{I_y}{2y^2W^2} - \frac{W_{yy}}{W}\right) = \frac{\partial^2}{\partial y^2} + P \tag{C.23}$$

and the corresponding boundary conditions are

$$\tilde{\phi}(0,z) = 0 \tag{C.24}$$
$$\tilde{\phi}(a,z) = 0. \tag{C.25}$$

For any realistic flow, coefficient P must be non-singular in $y = (0,a)$. According to the Sturm-Liouville theory [30], the solution to equation (C.22) can be expressed as an infinite set of eigenfunctions, orthogonal with respect to the weight, m. Each eigenfunction is scaled by an eigenvalue, $(\gamma_0^2 < \gamma_1^2 < \gamma_2^2 ...)$, which is real. Further, if γ in equation (C.21) is a pure imaginary ($\gamma = \imath\alpha$) it will be inversely proportional to the wavelength of a standing wave, i.e. $l = 2\pi/\alpha = i2\pi/\gamma$. The possibilities of standing waves in the flow are therefore limited to the set of eigenfunctions that have negative eigenvalues. If a standing wave is mathematically possible, the flow is referred to as *subcritical* and it will have at least one negative eigenvalue. If all eigenvalues are positive, the flow will be termed *supercritical*. Physically, a negative

eigenvalue, γ_0, means that the perturbation can propagate upstream. Consider a supercritical flow with a vortex breakdown far downstream at $z = 0$. Asymptotically, the upstream flow will experience the breakdown as a perturbation in the order of $\exp(-|\gamma_0 z|)$, since all following eigenfunctions will vanish more rapidly.

From Benjamin's theory, it is clear that the effects of a vortex breakdown will propagate upstream.

Appendix D

One Way to Visualize Vortices

There are various ways to visualize vortices. The most obvious method is to look at iso-surfaces of static pressure, because vortex cores are in general characterized by having a lower pressure than the surroundings. Hence, a bounded iso-surface of relatively low static pressure will often correspond to a vortex. However, iso-surfaces of static pressure will only visualize vortices having approximately the same core pressure. Strong vortices in regions of higher pressure can thus not be directly compared to equally strong vortices in low pressure regions. An alternative method that has been proven successful is to use the second invariant of the velocity gradient tensor, $II_{\partial_j u_i}$, see e.g. Jeong and Hussain [31]. It is in place to offer a physical interpretation of the scalar with such a long name.

D.1 The second invariant of the velocity gradient tensor

By taking the divergence of the incompressible Navier-Stokes equations,

$$\partial_i \left(\partial_0(\rho u_i) + \partial_j(\rho u_i u_j) \right) = \partial_i \left(-\partial_i p + \partial_j \left(\mu(\partial_j u_i + \partial_i u_j) \right) \right), \tag{D.1}$$

it follows that

$$\partial_j \partial_j p = 2\rho II_{\partial_j u_i}, \tag{D.2}$$

where

$$II_{\partial_j u_i} = 0.5 \left(\Omega_{ij}\Omega_{ij} - S_{ij}S_{ij} \right). \tag{D.3}$$

Here, $\Omega_{ij} = (\partial_j u_i - \partial_i u_j)/2$ is the rotation rate (vorticity) tensor and $S_{ij} = (\partial_j u_i + \partial_i u_j)/2$ is the strain-rate tensor.

The mathematical meaning of the second invariant of the strain rate tensor, $II_{\partial_j u_i}$, is thus that it constitutes the source term in the pressure equation for incompressible flow [31]. An iso-surface of this quantity can yield continuous structures that surround regions of the flow that influence the pressure equation in an equivalent way. The pressure equation, Eq. D.2, is an elliptic Poisson[1] equation. The local minimum of a solution to a Poisson equation can only occur if $II_{\partial_j u_i} > 0$. As the pressure level of a vortex core is generally lower than the surrounding pressure, the physical relation between a vortex and the positive values of $II_{\partial_j u_i}$ is obvious.

[1]Simon Denis Poisson, 1781-1840.

Appendix E

UDF

The source code of a commercial software is usually not available to the user. However, many commercial software programs admit the use of user defined functions (udf:s) to modify or complement the source code. The udf presented here is developed for the Fluent commercial software, version 6.3, and written in the C programming language. It shows how the filter function described by Gyllenram et al. [28] (Paper IV) is implemented and applied to the $k-\omega$ SST turbulence model [23, 22], which is one of many turbulence models available in Fluent. The subroutine `DEFINE_ADJUST` is called by the solver just before each iteration. It limits the eddy-viscosity used in the momentum equations not to be larger than $10^5 \times \mu$, where μ is the molecular viscosity. It also counts the number of cells in which the eddy-viscosity is limited and displays a warning in the command window of the software. The limiter is sometimes necessary to prevent divergence of the equations during the first iterations of a simulation. The filter itself could have been implemented in this subroutine and applied to the eddy-viscosity already implemented in the source code. However, because of the structure of the source code, that approach would end up in using different formulations of the eddy-viscosity for the momentum and turbulent transport equations. The filter function is instead computed together with the $k-\omega$ SST eddy-viscosity in the `DEFINE_TURBULENT_VISCOSITY` subroutine. This subroutine is in each iteration called by the solver directly after the momentum equations are solved, but prior to solving the transport equations for k and ω. The udf can be used in parallel as well as serial mode. The macros (field variables) used by the udf are listed below.

`C_K(c,t)`	Modelled turbulent kinetic energy, k
`C_MU_L(c,t)`	The field of molecular viscosity, μ
`C_O(c,t)`	Modelled specific dissipation rate, ω
`C_R(c,t)`	The density field, ρ
`C_U(c,t),C_V(c,t),C_W(c,t)`	Cartesian components of the resolved velocity vector, $\overline{u}_i$
`C_UDMI(c,t,0)`	The user defined memory allocation storing the modified eddy-viscosity, μ_t
`C_UDMI(c,t,1)`	The user defined memory allocation storing the filter function, g^2
`C_WALL_DIST(c,t)`	The distance to the nearest wall
`Strainrate_Mag(c,t)`	The magnitude of the resolved strain rate, $\sqrt{2S_{ij}S_{ij}}$

E.1 The eddy-viscosity of the filtered $k-\omega$ SST turbulence model

```
#include "udf.h"
#include "math.h"


DEFINE_ADJUST(trb_adj, domain)
{
   int nbnd=0;


   #if !RP_HOST /* ONLY SERIAL or NODE */


      Thread *t;
      cell_t c;


      thread_loop_c(t, domain)
      if (FLUID_THREAD_P(t))
      {
         begin_c_loop(c,t)
         {
            /* Limit unphysical eddy-viscosity */
```

```
            if (C_UDMI(c,t,0)>=100000.0*C_MU_L(c,t))
            {
               C_UDMI(c,t,0) = MIN(C_UDMI(c,t,0),
                  100000.0*C_MU_L(c,t));
               nbnd += 1;
            }
         }
         end_c_loop(c,t)
      }


      # if RP_NODE
         nbnd=PRF_GISUM1(nbnd);
      # endif /* RP_NODE */


   #endif /* !RP_HOST */


   node_to_host_int_1(nbnd);


   #if !RP_NODE /* ONLY SERIAL OR HOST */
      if (nbnd>0)
      {
         Message("WARNING! Turbulent to laminar viscosity
            ratio limited to 100,000 in %d cells \n",nbnd);
      }
   #endif /* !RP_NODE */


}


   DEFINE_TURBULENT_VISCOSITY(flt_mut,c,t)
{


   /* Define filter width */
   real alph=3.0;


   /* Define model constants */
   real bstarinf=0.09;
```

```
  real a1=0.31;
  real Lt,lt,VMAG,Dt,alphstar,dmp,F2,Phi2;
  Dt = RP_Get_Real("physical-time-step");


  /* Compute dynamic filter function */
  Lt=sqrt(C_K(c,t))/(bstarinf*C_O(c,t));
  VMAG=sqrt(SQR(C_U(c,t))+SQR(C_V(c,t))+SQR(C_W(c,t)));
  lt=alph*MAX(pow(C_VOLUME(c,t),1.0/3.0),VMAG*Dt);


  /* Store the filter function */
  C_UDMI(c,t,1)=SQR(MIN(pow(lt/Lt,2.0/3.0),1.0));


  /* Compute standard SST eddy-viscosity */
  Phi2=MAX(2.0*sqrt(C_K(c,t))/(bstarinf*C_O(c,t)*
    C_WALL_DIST(c,t)),500.0*C_MU_L(c,t)/(C_R(c,t)*
    SQR(C_WALL_DIST(c,t))*C_O(c,t)));
  F2=tanh(SQR(Phi2));
  /* alphstar only active in transitional version */
  alphstar=1.0;
  dmp=1.0/(MAX(1.0/alphstar,Strainrate_Mag(c,t)*
    F2/(a1*C_O(c,t))));


  /* Store the filtered SST eddy-viscosity */
  C_UDMI(c,t,0)=C_R(c,t)*C_UDMI(c,t,1)*C_K(c,t)*
    dmp/C_O(c,t);


  /* Return the filtered SST eddy-viscosity */
  return C_UDMI(c,t,0);
}
```

Appended Papers

Paper I W. Gyllenram, H. Nilsson and L. Davidson
"On the failure of the quasi-cylindrical approximation and the connection to vortex breakdown in turbulent swirling flow"
Physics of Fluids, 19:4, 2007.

Paper II W. Gyllenram and H. Nilsson
"Design and validation of a scale-adaptive filtering technique for LRN turbulence modeling of unsteady flow"
Accepted for publication in Journal of Fluids Engineering, 2008

Paper III W. Gyllenram and H. Nilsson
"The influence of boundary layers on the critical swirl level and stability of viscous swirling flow"
Submitted to scientific journal, April 2008.

Paper IV W. Gyllenram, P. Stein and H. Nilsson
"Assessment of a hybrid LES/RANS turbulence model in unsteady swirling and recirculating flow"
Submitted to scientific journal, April 2008.